POLITECNICO
MILANO 1863

SCUOLA DI INGEGNERIA INDUSTRIALE
E DELL'INFORMAZIONE

Solution processed cation doped CZTS photocathode for PEC devices

TESI DI LAUREA MAGISTRALE IN
MATERIALS ENGINEERING AND NANOTECHNOLOGY -
INGEGNERIA DEI MATERIALI E DELLE NANOTECNOLOGIE

Author: **Oscar Arnulfo Núñez Rincón**

Student ID: 10683381
Advisor: Luca Magagnin
Co-advisor: Ruben Dell'Oro
Academic Year: 2021-2022

Acknowledgments

I would like to thank the following people for helping with this adventure, without whom I would not have been able to complete this master's degree.

Professor Luca Magagnin and Ruben Dell'Oro for your total willingness to help me achieve my objectives in favor of scientific advancement, for your dedication, always putting solutions before problems, and with the best attitude to train me as a better material's engineer for tomorrow.

María Paula Ospina, for always motivating me to be a better person, for accompanying me in all my sacrifices, and for the ones you did too, thank you for all your essential support.

To my colleagues from Camplus Lambrate residence, Joey, Hugo, Luis, Marat, David, and also to Paulina for allowing me to live this experience to the fullest, for helping me understand that there is always a reason to be happy no matter what is happening around us.

My family, for prompting me to dream big and learn that we are here to help each other, that we are making these sacrifices for a better world. Without your company, none of this grandiose achievement would have been possible.

Finally, to all those people who made my stay in Milan the most important experience of my life, to Politecnico di Milano for teaching me to love what I do and for giving me the tools to continue growing professionally, I hope we can meet again in the future.

Abstract

In this thesis work, the effect of cadmium doping on copper zinc tin sulfide Cu_2ZnSnS_4 (CZTS) was investigated for water splitting application in a photoelectrochemical cell. The aim is to design a replicable photocathode without expensive elements thinking on a future large-scale production. CZTS is a promising photoabsorber for water reduction to produce hydrogen due to its optical properties, but the high presence of defects limits its performance. For the improvement of the bulk properties, Zn was partially replaced with Cd to prepare a pure sulfide CCZTS via sol-gel method using spin coating. CdS was applied as buffer layer by chemical bath deposition (CBD), and Pt was used as catalyst through 10-30 min photo electrodeposition (PED).

XRD was used together with SEM-EDS for the material characterization. A shift in the (112) XRD peak was found coming from a 17% crystallite size expansion and a grain size increase from 100nm to 200nm. Linear Scan Voltammetry (LSV) tests were carried out in a solution containing 0.5 M phosphate buffer and 0.5 M Na_2SO_4 at pH 7. Samples were illuminated from the front and backside with the solar simulator to deliver an AM1.5.

CCZTS photoelectrochemical performance shows an enhancement of photocurrent density up to 73.86% compared to the undoped CZTS. The doped material improves its performance when increasing the number of spin coated layers in front illumination, reaching its maximum with 13 layers (-8.18 mA/cm^2 at 0V vs. RHE). The situation was inverse in back illumination due to the shorter path that the main carriers must follow to the surface, achieving its best performance with 2 layers (-2.96mA/cm^2 at 0V vs. RHE). Pt PED must be controlled, obtaining the best results with 20min deposition time especially in back illumination. Finally, maximum 1.68% at 0.74V applied bias was obtained, showing that although the material can be improved, it is a good starting point for H_2 generation.

Key-words: Photoelectrochemical water splitting, CZTS, Cd doping, Pt photo electrodeposition, PEC device.

Abstract in lingua italiana

In questo lavoro di tesi sono stati studiati gli effetti del doping con cadmio del solfuro di rame zinco e stagno Cu_2ZnSnS_4 (CZTS) applicato alla scissione dell'acqua in una cella fotoelettrochimica. L'obiettivo è stato la progettazione un fotocatodo senza elementi costosi o tossici pensando a una futura produzione su larga scala. Il CZTS è un promettente photoabsorber per la riduzione dell'acqua ad idrogeno grazie alle sue proprietà ottiche, ma l'elevata presenza di difetti ne limita le prestazioni. Per migliorare le proprietà, lo Zn è stato parzialmente sostituito con Cd per preparare il materiale dopato CCZTS tramite metodo sol-gel via spin coating. CdS è stato applicato come buffer layer mediante deposizione in bagno chimico e il Pt è stato utilizzato come catalizzatore attraverso 10-30 minuti di fotoelettrodeposizione (PED) studiata.

XRD è stata utilizzata insieme a SEM-EDS per la caratterizzazione del materiale. È stato riscontrato uno spostamento nel picco XRD (112) derivante da un'espansione dei cristalliti del 17% e un aumento dei grani da 100 nm a 200 nm. I test di Voltammetria a Scansione Lineare sono stati eseguiti in una soluzione tampone di fosfati 0,5 M contenente Na2SO4 0,5 M a pH 7. I campioni sono stati illuminati dalla parte anteriore e posteriore con il simulatore solare per fornire un AM1.5.

Le prestazioni fotoelettrochimiche CCZTS mostrano un miglioramento della densità della fotocorrente del 73.86% rispetto al CZTS non drogato. Il materiale drogato migliora la sua performance all'aumento del numero di strati depositati per spin coating quando illuminato frontalmente, raggiungendo un massimo a 13 strati (-8.18 mA/cm^2 a 0 V vs. RHE). La dipendenza si presenta inversa in caso di retroilluminazione a causa del minor percorso che i portatori di carica devono percorrere per raggiungere la superficie, ottenendo la prestazione più elevata con 2 soli strati (-2.96 mA/cm^2 a 0 V vs. RHE). L'eletrodeposizione fotoassistita di Pt ha mostrato di richiedere un certo controllo, ottenendo un miglior risultato per un tempo di deposizione di 20 min, specialmente per condizioni di retroilluminazione. In conclusione, è stato ottenuto un massimo di efficienza sotto tensione applicata (ABPE) di 1.68% a 0.74 V, mostrando che, pur con un margine di miglioramento sulla qualità del materiale, il fotoelettrodo costuisce un buon punto di partenza per la produzione di H2.

Parole chiave: Scissione fotoelettrochimica dell'acqua, CZTS, drogaggio con Cd, fotoelettrodeposizione di Pt, dispositivo fotoelettrochimico

Contents

1. Introduction

1.1   Energy in the world

The net global energy related CO_2 emissions in 2020 flattened at around 31.3Gt, showing a reduction of 5.8% respect to the previous year and after two years of increasing. Although it is the largest percentage decrease since World War II, it was due to the 4% primary energy demand worldwide. Apparently, this is a good reason, but the changes produced by the COVID-19 pandemic situation and its consequences in the industry and the lower use of oil for transport cannot be ignored. As the situation improves, travel and economic activities pick up around the world, oil consumption and its emissions are rising again. [1].

COVID-19 reduced electricity demand 20% on average every month of lockdown. The global electricity demand decreased 2.5% in the first quarter of 2020, and demand for oil and coal fell nearly 5% and 8% respectively [2]. After reading this, you must be thinking that we are not just improving but the world is forcing us too. The Energy production and use account for more than two-thirds of global greenhouse gas emissions [3], and this is the reason for what renewables energies sources must be implemented and improved, because taken together them with the energy efficiency measures, they can achieve most of the carbon reductions required to keep global temperature rise below 1.5 degrees Celsius.

In 2019, renewable energy installed power capacity increased more than 200 gigawatts (GW), it was the highest increase ever, but in 2021 more than 256GW of renewable power capacity was added globally during the year, surpassing the previous record by nearly 30%, also, 77 countries, 10 regions and more than 100 cities announced their commitment to net zero carbon emissions by 2050. [2]. However, the use of renewable energy alone is not enough, and it is not a matter of simply reduce the consumption of

energy. The energy optimization is influenced by first, technology and design reaching higher energy efficiencies. Second, structural changes, or changes in the composition of sectors or within a sector which can be achieved through investments, policies, and planning processes [4]. Finally, with energy conservation measures, and this is our role because it depends on the behaviors and habits of energy end-users.

1.2   Hydrogen

Hydrogen is highly versatile and can be used both as a feedstock and as an energy source. It is widely employed in the chemical industry as reducing agent for the synthesis of different chemical compounds. Today, it is mainly used as a feedstock for industrial processes, including ammonia production for fertilizer (50%), in refining (35%) as well as for the food, electronics, glass and metal industries [5]. However, as energy leaders seek solutions for decarbonization, hydrogen as an energy vector is gaining force.

With the aim of improving the first factor of energy optimization related to technology and design, hydrogen industry appears as the perfect fuel. It is the most abundant element on the earth, can be stored in gaseous or liquid state, can be transported by gas pipelines, replacing natural gas, can give more than 3 times the energy per liter than diesel or natural gas, and does not emit greenhouse gasses during its combustion. However, it is not all good news, the current cost, and the difficulties in the production of hydrogen make it difficult to use this element as a 100% renewable energy source nowadays.

Why if hydrogen is the most abundant element of the earth, we cannot simply use it as energy source? Because Hydrogen is not easy to obtain, since it is not found alone in nature, but is generated from other substances that contain it, including water, coal, and natural gas. For this reason, hydrogen production is classified in colors depending on the energy source according to the figure 1.

	Terminology	Technology	Feedstock/ Electricity source	GHG footprint*
PRODUCTION VIA ELECTRICITY	Green Hydrogen	Electrolysis	Wind | Solar | Hydro Geothermal | Tidal	Minimal
	Purple/Pink Hydrogen		Nuclear	
	Yellow Hydrogen		Mixed-origin grid energy	Medium
PRODUCTION VIA FOSSIL FUELS	Blue Hydrogen	Natural gas reforming + CCUS Gasification + CCUS	Natural gas | coal	Low
	Turquoise Hydrogen	Pyrolysis	Natural gas	Solid carbon (by-product)
	Grey Hydrogen	Natural gas reforming		Medium
	Brown Hydrogen	Gasification	Brown coal (lignite)	High
	Black Hydrogen		Black coal	

*GHG footprint given as a general guide but it is accepted that each category can be higher in some cases.

Figure 1. Color classification of Hydrogen as energy source. [6]

In Europe, the EU introduced a new hydrogen strategy, including a goal of 6 GW of electrolyser capacity powered by renewable electricity by 2024 and 40 GW of renewable hydrogen electrolyser capacity by 2030 [2]. Therefore, nowadays the research is going through find solutions to achieve the green hydrogen as one of the main energy sources for the future.

Green Hydrogen is produced through renewables driven electrolysis or gasification using renewable feedstocks. In this way, hydrogen can be directly combusted for use in transport, heat, or used to generate electricity via fuel cells.

This work will be focused on Photoelectrochemical water splitting, one way to produce green hydrogen. Specifically on the doping of Cu_2ZnSnS_4 (CZTS) spin coated semiconductor as photocathode for solar water splitting, also discussing the parameters that modify front and back illumination.
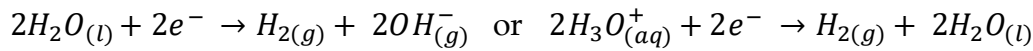
1.3   Water Electrolysis

Water electrolysis was first demonstrated in 1800 by William Nicholson and Sir Anthony Carlisle, it is the process of using electricity for splitting water into hydrogen and oxygen through the application of electrical energy, this process follows the equation 1.

4

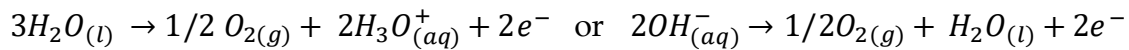$$H_2O + electricity \rightarrow H_2 + {}^1\!/_2\,O_2$$
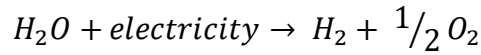
At room temperature this reaction is not spontaneous, on the contrary, if we keep increasing the temperature the reaction becomes spontaneous and the equilibrium conversion increases because the reaction is endothermic. The system is made using a power supply, a cathode, an anode, and the electrolyte.

A DC current is applied from the negative terminal of the power source to the cathode, where the hydrogen is produced. At the anode, the electrons produced by the electrochemical reaction return to the positive terminal of the DC source. The overall water splitting reaction is divided into two half reactions that take place at two different interfaces.

1. Hydrogen reaction evolution (HER)

$$2H_2O_{(l)} + 2e^- \rightarrow H_{2(g)} + 2OH^-_{(g)} \quad \text{or} \quad 2H_3O^+_{(aq)} + 2e^- \rightarrow H_{2(g)} + 2H_2O_{(l)}$$

2. The oxygen evolution reaction (OER)

$$3H_2O_{(l)} \rightarrow 1/2\,O_{2(g)} + 2H_3O^+_{(aq)} + 2e^- \quad \text{or} \quad 2OH^-_{(aq)} \rightarrow 1/2O_{2(g)} + H_2O_{(l)} + 2e^-$$

HER is the reaction where water is reduced at the cathode to produce H_2, so it is giving electrons to the molecules, and OER is the reaction where water is oxidized at the anode to produce O_2, so, at the anode electrons are extracted from the molecules. To close the circuit and allow the passage of charges without accumulation, the two electrodes must be linked by an ionic conductor, which is a medium that allows the passage of ions but not free electrons. One of the critical issues that avoid the practical use of water splitting is the sluggish reaction kinetics of HER and OER due to high overpotentials [7], a measure of the kinetic energy barriers. Catalysts are required to minimize the overpotentials towards efficient H_2 and O_2 production.

The electrolyte can be made of a proton exchange membrane (PEM), an aqueous solution containing ions, or by an oxygen ion exchange ceramic membrane as shown in figure 2.
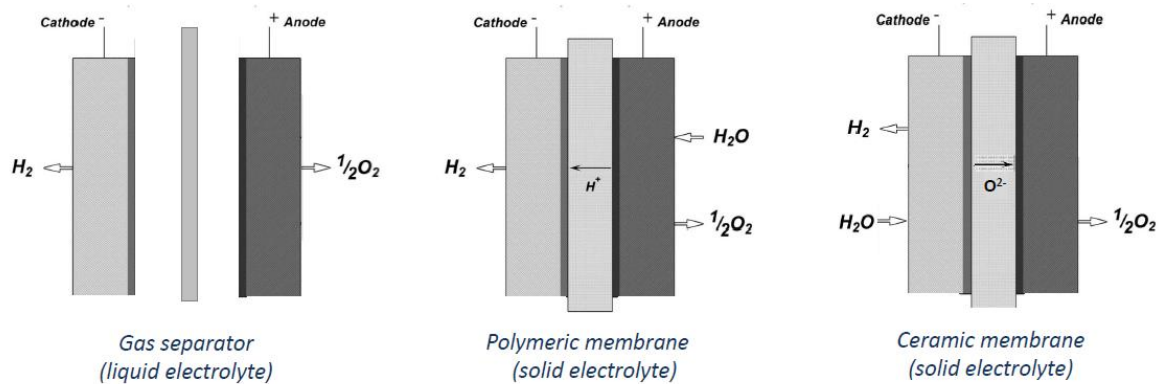

Figure 2. Water electrolysis technologies. [8]

The left one is the conventional electrochemical cell and consists of a cathodic and anodic region separated by a diaphragm. The electrolyte employed is typically 20%-40% KOH aqueous solution, KOH increases the electrolyte conductivity lowering the ohmic drops. Moreover, the higher amount of OH^- reduces the overpotential for the oxygen evolution reaction. In the PEM, a solid electrolyte physically separate cathode and anode allowing only the passage of H^+ species. The PEM is normally made of fluorinated polymer typically Nafion and must be mechanically stable to sustain the high pressure in the cell, de-ionized water is employed. Finally, in the ceramic membrane a solid oxide diaphragm physically separate cathode and anode allowing the passage of O^{2-} species only. More detailed information is given in table 1.

Table 1. Information of water electrolysis technologies. [8]

Water electrolysis technologies		
Alkaline cell electrolyser	**PEM electrolyser**	**Solid oxide electrolyser cell**
Cathodic reaction $2H_2O + 2e^- \rightarrow H_2 + 2OH^-$	$2H^+ + 2e^- \rightarrow H_2$	$H_2O + 2e^- \rightarrow H_2 + O_2^-$
Anodic reaction $2OH^- \rightarrow 1/2O_2 + H_2O + 2e^-$	$H_2O \rightarrow 1/2O_2 + 2H^+ + 2e^-$	$O_2^- \rightarrow 1/2O_2 + 2e^-$
Cathodic material **Stainless steel + Pt(Catalyst)**	**Carbon + Pt(Catalyst)**	**Ni-YSZ**
Anodic material **Ti/Ni + Ni/Co/Fe(catalyst)**	**Titanium + Ir(catalyst)**	**YSZ/ScSZ**
Electrolytic material **20-40% KOH aqueous solution**	**Sulfonated tetrafluoroethylene**	**$La_{1-x}Sr_xMnO_3$**
Temperature (°C) **70-80**	**60-80**	**700-1000**
Current density (mA/cm²) **200-400**	**600-1000**	**up to 1000**
H₂ generation capacity (Nm³/h) **1-800**	**up to 10**	**research state**
Electric power **5kW - 3.4MW**	**0.1kW - 100kW**	**research state**

2. State of art

2.1 Conductors, semiconductors, and insulators

The electronic properties of materials are important because depending on the type of material we can have different absorption of photons and so, give different level of energy to the system. Electrical conductivity is an interesting property of the solid materials, it is a huge range where on one side there are the conductors with high conductivity, on the other side materials called insulators with low conductivity, and semiconductors in an intermediate region between these two. Although the electrical conductivity of semiconductors is much less than the one of metals, here this property increases with the temperature while on the metals it decreases.

To explain the difference of these three types of materials we can start from the band theory and definition of the bands. In a solid, electrons rather than having distinct energy levels, their behavior is related to the behavior of all other particles around it, and so the energy states form bands. There exist some allowed and forbidden bands, the former are the valence and the conduction band, and the forbidden band is the difference between the previous two, called energy band gap. The valence band (VB) is the highest range of electron energies in which electrons are normally present at absolute zero temperature. The conduction band (CB) is the band of electron orbitals that electrons can bounce up into from the VB when energized. The difference between the highest and lowest occupied single-particle states in a quantum system of non-interacting fermions at absolute zero temperature is called Fermi Energy [9]. The Fermi level is the highest energy level that an electron can occupy at the absolute zero temperature.

In a metal, either the conduction band is partly filled, or no separate conduction and valence band exist, electrons can move freely, the resistivity increases with the temperature and the electrons give their energy to the photons very fast. In the case of

8

insulators, the distance between the valence band and the conduction band (Energy band gap) is so high (Egap>3eV) that usually no conductivity despite doping is possible. Then, there exist the semiconductors which are insulators at low temperature, conduction band at low temperatures is almost empty, valence band is almost full, the band gap is between 0.1eV and 3eV so it is possible to have conductivity with higher temperatures. See figure 3. Conductors, semiconductors, and insulators energy bands.
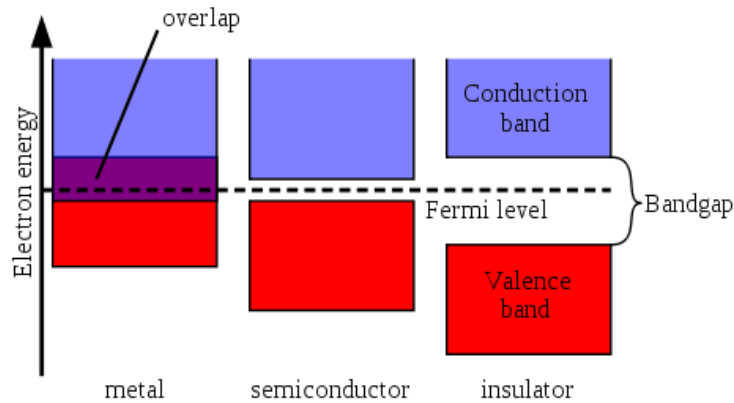

Figure 3. Conductors, semiconductors, and insulators energy bands.[10]

2.2 Electrons and light

To create green energy, the aim is to be able to perform the water electrolysis using renewables sources. It means that the energy provided to the system, and so, the electrons travelling inside the system allowing the reactions previously shown in the section 1.3, are produced by clean energy. One way, to achieve it is through the solar energy and separation of charges. This method will be introduced in section 2 but the point is that the photons can interact with the electrons giving energy. This energy absorbed by the electrons will excite them to higher energy levels where charges can be extracted.

The energy that a photon can give to an electron and cause the excitation process follows the Plank-Einstein relation:

$$E = h\nu$$

Where E is the energy, h is the Plank's constant $6,626×10^{-34}$ J*s, and ν is the frequency, in this case, the frequency of the monochromatic light. However, E is only the energy carried by a photon, but it is not sure that the electron will be excited because it needs to overcome the forbidden energy gap. So, an electron will be excited to the CB only if the energy is equal or higher than the Egap.

Absorption is the transition stimulated by a photon from a vibrational level of the ground state to a certain vibrational level of an excited electronic state. This is a very fast process, with characteristic time of femtoseconds (10^{-15}s). Due to this short characteristic time for the absorption process to occur, no concomitant displacement of the nuclei is observed during absorption (this is known as Franck-Condon principle). The higher the energy gap between the ground and the excited state, the lower the wavelength (λ) to be absorbed.

Once the electron is at the excited state, it can experience relaxation or recombination. Relaxation is the transition to a lower vibrational level inside the same electronic state. This is a non-radiative mechanism meaning that no photons are emitted because of it. In this part of the process there are the electron and phonon collisions, electrons and holes lose energy because they are giving it to the lattice. Relaxation lasts from picoseconds (10^{-12}s) to femtoseconds. Finally, the recombination occurs when an electron jumps back to the valence band and recombine with a hole, this step lasts from microseconds (10^{-6}s) to nanoseconds (10^{-9}s). Fortunately, the recombination is slower than absorption and the aim is to separate the charges before the first occurs.

Semiconductors are used for these purposes because they give this time slot for the separation of charges to be achieved. Conductors do not even have a band gap, so it seems to be the perfect condition because they absorb all the photons, but in that case the absorption is useless due to the immediate relaxation to the original level thanks to the continuity of the energy levels, it means that if the band gap does not exist, electrons cannot keep the energy that they get from photons and there will not be generation of a current. On the contrary if the band gap does not exist, or if it is too large as in insulators, no absorption will be possible and so neither will be the generation of current.

2.3 Energy levels and conductivity in a semiconductor

At T=0K, all the electrons occupy the lowest possible states in a pure semiconductor. It means that the CB is completely empty while the VB es full of electrons. In this case, the Fermi energy level is at the Egap.

At T>0K, higher energy levels start to be occupied due to the excitation of some electrons, and with the increase of temperature, the increase in the probability to find an electron in a higher energy level. This probability of an electron occupying an energy level E varies with $e^{-E/k_B T}$[11].

At thermodynamic equilibrium, probability of finding an electron at the energy level E is given by the Fermi-Dirac probability distribution $f(E)$.

$$f(E) = \frac{1}{1 + e^{(E-E_F)/k_B T}}$$

where E is the energy level of interest, EF is the Fermi level, T is the absolute temperature, and k_B is Boltzmann's constant ($1.38*10^{-23}$J/K).

For low temperatures, the fermi distribution is a step function that is nearly 1 if $E < E_F$ and nearly 0 if $E > E_F$. This means that the particles are placing from the lowest energy level upwards due to the Pauli Exclusion Principle until all the particles have been placed. The energy of the last occupied level is called Fermi energy and the temperature to which this energy corresponds is called Fermi Temperature, calculated as $E_F = k_B T_F$.
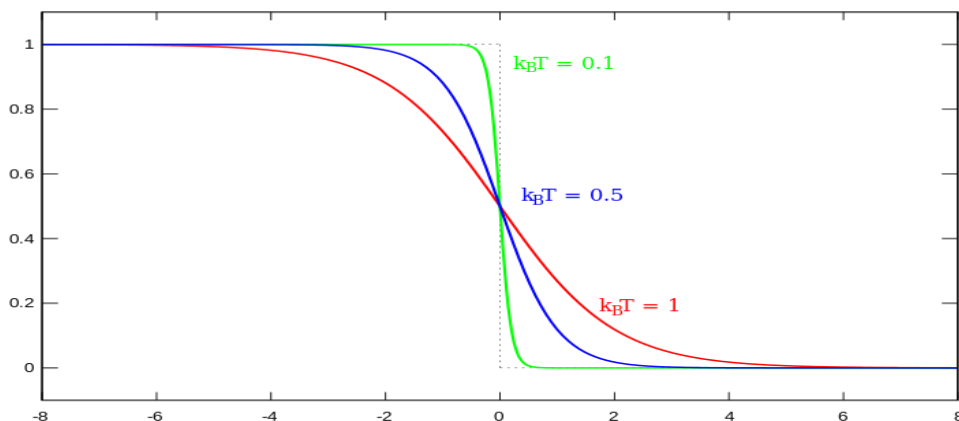

Figure 4. Schematic plot of Fermi-Dirac distribution. [12]

What its important is that at absolute zero temperature, the behavior is like an insulator because there are no free carriers available, situation that change increasing the temperature. It is important to notice that here the holes play an important role as they can also be referred as carrier of electricity, and in an ideal semiconductor crystal number of holes created per unit time is equal to the number of movements of electrons to a new site. This rate of creation of electron-hole pair increases when temperature increases, and when the temperature decreases, the rate electron-hole pairs is reduced due to recombination in the crystal.

Electrical conductivity is defined as "The rate of charge flow across unit area in a conductor per unit potential (voltage) gradient", thus, it depends on the mobility of the carriers μ_h and μ_e, the charge e, and the concentration of carriers p and n.

The mobility is defined as:

$$\mu = \frac{e\tau}{m^*}$$

Where, τ is the mean free time of recombination and m^* is the effective mass. Thus, the drift current densities are given by:

$$J_h = ep\mu_h E \qquad J_e = en\mu_e E$$

And finally, the electrical conductivity is calculated as:

$$\sigma = \sigma_e + \sigma_h = e(n\mu_e + p\mu_h)$$

2.4 Doping

The electrical resistivity (conductivity) of a semiconductor can be changed by doping by several orders of magnitude, over eight orders in the case of Silicon. A striking property of these elements is that their conductivities increase abruptly when they are doped with small quantities of other elements. Doped semiconductors are called Extrinsic and doping is the introduction of impurities into a semiconductor crystal for a defined modification of conductivity [8].

N-type material is created when group V atoms area added to semiconductor materials from group IV, so that the extra valence electron is free to participate in conduction.

Therefore, more electrons are added to the conduction band increasing the number of electrons present, consequently improving the conductivity of a semiconductor.

P-type materials are created when semiconductor materials from group IV are doped with group III atoms for example when silicon is doped with boron, increasing the conductivity due to the increase in the number of holes.

Doping will change the Fermi level. Too see how let's start by finding the initial position of the fermi level. First, the density of states (g(E)) is the number of states per interval of energy at each energy level that are available to be occupied by electrons:

$$g_C(E) = \frac{(2m_e^*)^{3/2}}{2\pi^2\hbar^3}\sqrt{E - E_C} \qquad\qquad g_V(E) = \frac{(2m_h^*)^{3/2}}{2\pi^2\hbar^3}\sqrt{E_V - E}$$

Where Ec and Ev are the energies at the CB edge and VB edge respectively. Now, the CB electron density (n) and VB hole density (p) can be found as the multiplication of this number of states available by a probability that tells us the portion of those states which will actually have electrons in them (Fermi-Dirac Distribution):

$$n = \int_{E_C}^{+\infty} g_C(E)f(E,T)dE \qquad\qquad p = \int_{-\infty}^{E_V} g_V(E)[1 - f(E,T)]dE$$

Considering that:

$$\frac{1}{\exp\left[(E - E_F)/kT\right] + 1} \approx \exp\left(-\frac{E - E_F}{kT}\right) \quad for\ E - E_F \gg 2kT$$

The carrier densities will be:

$$n = 2\left(\frac{2\pi m_e^* kT}{\hbar^2}\right)^{3/2} \exp\left(-\frac{E_C - E_F}{kT}\right) = N_{eff}^C \exp\left(-\frac{E_C - E_F}{kT}\right)$$

$$p = 2\left(\frac{2\pi m_h^* kT}{\hbar^2}\right)^{3/2} \exp\left(\frac{E_V - E_F}{kT}\right) = N_{eff}^V \exp\left(\frac{E_V - E_F}{kT}\right)$$

The mass action law states that the number of electrons in CB and the holes in VB is constant at a fixed temperature and is independent of amount of donor and acceptor impurity added.

$$mass\ action\ law \quad np = 4\left(\frac{kT}{2\pi\hbar^2}\right)^3 (m_e^* m_h^*)^{3/2} e^{-E_g/kT}$$

In the case of intrinsic semiconductor, considering that n=p:

$$E_F = \frac{E_C + E_V}{2} + \frac{kT}{2}\ln\left(N_{eff}^V/N_{eff}^C\right)$$

And in this point, it is clear that at T=0K, the E_F will be in the middle of the gap. But for a doped semiconductor the fermi level is moving upwards with n doping and downwards with p doping

However, the assumption of a unique Fermi level not always hold. A semiconductor under illumination is not at thermodynamic equilibrium, the concentration of electrons and holes is increased by light absorption and so they cannot be described by the same Fermi function because under non-thermal equilibrium the product of electron and hole concentration is larger (generation of carriers) or smaller (recombination of carriers) than the square of the intrinsic carrier concentration. In this point we speak about quasi-Fermi levels, one for electrons that are near the Ec ($E_{F,p}$) and one for holes near the Ev ($E_{F,n}$).

$$n-type \quad n = N_D, \quad p = \frac{n_i^2}{N_D} \quad E_{F,n} = E_i + kTln\frac{n}{n_i} \approx E_i + kTln\frac{N_D}{n_i}$$

$$p - type \qquad p = N_A, \qquad n = \frac{n_i^2}{N_A} \qquad E_{F,p} = E_i - kT ln \frac{p}{n_i} \approx E_i - kT ln \frac{N_A}{n_i}$$

Where n_i and E_i are the carrier concentration and Fermi energy level in the undoped semiconductor, N_D and N_A are the concentration of donor and acceptor atoms.
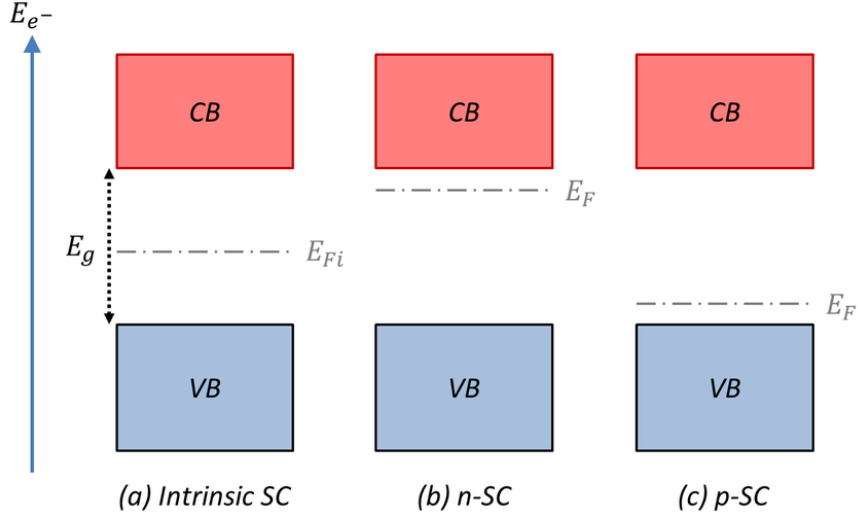

Figure 5. Energy band diagrams for (a) an intrinsic semiconductor, (b) an n-doped one, and (c) a p-doped one. [13]

2.5 The semiconductor-electrolyte interface

To measure the electrochemical potential of electrons in a redox electrolyte, physics has adopted the electron energy in vacuum as reference, whereas electrochemists have traditionally used the standard hydrogen electrode (SHE) scale. The zero of SHE scale appears to lie at −4.5 eV with respect to the vacuum level. The relation between redox potential E_{redox} (as defined with reference to SHE) with the Fermi level $E_{F_{redox}}$ [14].

$$E_{F_{redox}} = -4.5eV - e_o E_{redox}$$

This is because to measure the free energy of electrons within a solid, physicists often employ the concept of work function ($\chi = e_o \phi$; where ϕ is the electric potential below the vacuum level and e_o is the elementary charge of an electron), which represents the

energy needed to liberate a bound electron to the level of vacuum ($\phi_{vac} = 0$). By contrast, electrochemists used the concept of electrochemical potential to measure the free energy of charges.

When a semiconductor is brought into contact with an electrolyte, a potential difference is established at the interface and electrostatic adjustment occurs at the semiconductor-electrolyte interface, electrons flow from the phase of more negative E_F to the other to attain equilibrium, in which the semiconductor E_F matches the electrolyte $E_{F_{redox}}$ causing the formation of the space charge region. Consider the case of an n-type semiconductor and let $\varphi(x)$ be the variation of the electrostatic potential, we set $\varphi = 0$ in the bulk of the semiconductor. If the value φ_s of the potential at the surface is positive, the bands band downwards, and the concentration of electrons in the conduction band is enhanced forming the enrichment layer. If $\varphi_s < 0$, the bands bend upward, and the concentration of electrons at the surface is reduced; we speak of a depletion layer. the same terminology is applied to the surface of p-type semiconductors. So, if the bands bend upward, we speak of an enrichment layer; if they bend downward, of a depletion layer [15]

This depletion layer contributes to an internal electric field in the semiconductor and the majority carriers are forced away from the interface. For the equilibrium of this interface the flow of charge from one phase to the other is needed and a band bending occurs within the semiconductor phase. The magnitude and direction of band bending can simply be adjusted by an externally applied potential.

The special potential at which the electrostatic potential is constant, is the flat-band potential, which is equivalent to the potential of zero charge.
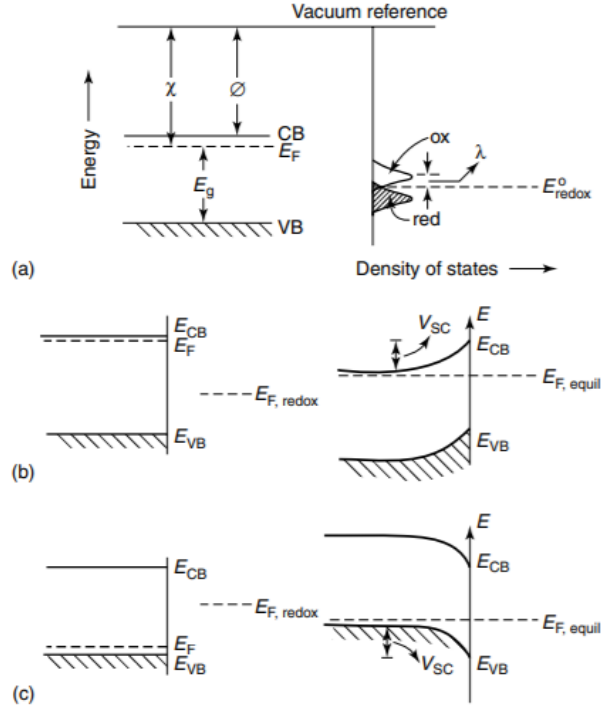
Figure 6. a) Energy levels in a semiconductor (left-hand side) and a redox electrolyte (right-hand side). φ and χ are the work function and semiconductor electron affinity, respectively. (b) The semiconductor-electrolyte interface before (LHS) and after (RHS) equilibration shown for a n-type semiconductor. (c) Same as (b) but for a p-type semiconductor. [12].

The difference between the Fermi levels of the semiconductor and of the redox couple before contact will determine the Band bending at equilibrium. The Fermi level is directly proportional to the electrode potential, which means that the final voltage across the interface can be controlled. [16]

The depletion width (W_{sc}) is the distance far away from the surface at which the depletion of electrons near the surface diminishes. This W_{sc} can be calculated based on the dielectric constant of the semiconductor, the carrier concentration, and the difference of the fermi level (in vacuum) as mentioned before, as:

$$W_{sc} = \sqrt{\frac{2\varepsilon_0\varepsilon_{SC}}{qN}\left(\Delta\phi_{SC} - \frac{kT}{q}\right)}$$

Where N is the carrier concentration, $\varepsilon_0\varepsilon_{SC}$ are the permittivity in vacuum and the dielectric constant of the semiconductor, and $\Delta\phi_{SC} = \phi_{F,SC} - \phi_{F,redox}$. In resume, the

extend of band bending depend on the applied potential because $\phi_{F,SC}$ equals the applied potential. Why this bending is so important for the green energy generation? Because as it is mentioned above, the idea is to generate hydrogen using renewable energy sources, one of these sources is the sunlight (Photovoltaic), and the built-in formed by the band bending is crucial for the photoelectrochemical water splitting because it is the driving force for charge separation at the semiconductor/electrolyte interface that will allow the generation of hydrogen and oxygen. This process is called Photoelectrochemical water splitting and is the topic in which this work will be center in.

2.6 Photoelectrochemical water splitting (PEC)

There are four main ways to produce hydrogen, by thermal processes where heat, in combination with closed-chemical cycles, produces hydrogen from feedstocks (gas reforming, coal gasification, biomass gasification, solar thermochemical hydrogen (STCH). Using biological processes, in which Microbes such as bacteria and microalgae can produce hydrogen through biological reactions, using sunlight or organic matter (microbial biomass conversion and photobiological water splitting). Third, by electrolytic processes using electricity to split water into hydrogen and oxygen (water electrolysis) in an electrochemical cell. And finally, by photolytic processes, splitting water into hydrogen and oxygen by means of light energy (photons) and a photoactive material (photoelectrochemical water splitting).

The photoelectrochemical water splitting (PEC) is a result of integrated solar energy conversion and water electrolysis in a single photocell. It uses semiconductor materials immersed in a water-based electrolyte to convert solar energy directly to chemical energy in the form of hydrogen. PEC is a promising technology that utilizing 36,000 TW of solar power, a conversion of 1% of the available solar energy, and PEC cell with 10% efficiency, could produce 36 TW power, the predicted global energy consumption in the year 2050 [17]. The chemical process is shown in the equation 1.

$$H_2O + 2h^+ + 2e^- \rightarrow H_2 + \frac{1}{2}O_2$$
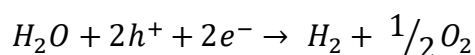
Electrolysis is a photoinduced reaction processes at the interface between a semiconductor material and the electrolyte solution, which requires a minimum Gibbs free energy of 237 kJ/mol. The catalyst is directly integrated onto the photoabsorber material, immersed in the solution. So, photo-active semiconductor, usually a transition metal oxide, is immersed in water and the photo-generated electrons and holes are directly used to split water. Upon illumination, electrons are excited in the conduction band, while holes form in the valence band. The formation of a junction between the semiconductor material and the electrolyte allows the charge separation after excitation as follows:
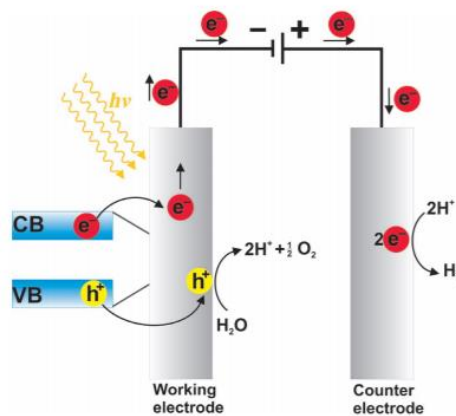
Figure 7. Working principle and basic configuration of a PEC cell. [18]

PEC cell is made by the working electrode, the counter electrode, one or both being photoactive (photoelectrode). Sometimes also contains a reference electrode to observe half reactions in the cell [19]. This electrode system is mainly immersed in an aqueous electrolyte.

In n-type semiconductors, electrons are collected at the photo anode and transported through the external circuit to the counter electrode. The electrons are consumed in the reduction of H^+ to H_2 that occurs at the cathode, on the other hand, the function of the holes is to oxidize the water into O_2 and H^+ at the anode. If the semiconductor used is a p type, the photo generated electrons are used to reduce H^+ in H_2, while in the counter electrode, the water is oxidized to O_2 and H^+. [20]

2.6.1 Photoelectrode requirements

Under standard temperature and pressure conditions, the water splitting process is not spontaneous, which is why a necessary potential difference must be applied. For this reason, the most important aspect is selecting the photoanode and photocathode materials, so, semiconductors with a suitable band gap and energy levels are extremely necessary to increase the spontaneity of the reaction.

First, it is important to select the appropriate band gap energy and positions. Sunlight consists of 52% infrared radiation (700–2500 nm), 43% visible (400–700 nm), and 5% UV (300–400 nm). Thus, it is needed to have a good light absorption in the visible region. Consequently, considering the proton reduction potential (0V vs SHE) and the O_2/H_2O potential (1.23 SHE), the band gap in ideal conditions will be 1.23eV which corresponds to 1100nm of wavelength. However, this analysis does not consider neither the overpotential requirement for acceptable surface reaction kinetics (0.4–0.6 eV) nor the energy losses by thermodynamics that are in the range of 0.4eV. Thus, the minimum band gap for the reactions to occur is ~1.8eV (700nm). But this was only considering the band gap and not the position, E_v of photoanode should be higher than 1.23V allowing the OER reaction to occur, E_c of cathode should be less than 0V favoring the HER reaction, and ideally, the upper limit should be 3.2eV because there is a rapid drop in sunlight intensity at 390nm. In summary, for a single semiconductor, the band gap should be between 1.8eV-3.2eV. There is the need of high photovoltage to separate the charges, so, tandem (see next section) or external biased devices are needed to provide the extra voltage.

In second place, the recombination is one of the main causes of low efficiency. Outstanding charge carrier separation and transportation are fundamental, thus, mobilities should be high enough but also the crystallinity and nanostructure must be taken into account avoiding the recombination centers. This recombination can be asset by the lifetime of carriers or using the diffusion length, in any case, they are related through the following equation:

$$L_D \approx \sqrt{D\tau}$$

In which L_D is the diffusion length expressing the average length a carrier moves between generation and recombination, τ is the time it takes an electron before

recombining, and D is the diffusivity, that is a measure of how quickly a group of particles fill a space and it is calculated using the intrinsic mobility μ by:

$$D = \frac{kT\mu}{e}$$

Third, surface catalytic activity because it will lead to sufficiently fast surface reaction kinetics that can prevent recombination by charge accumulation at the surface. Additionally, stability plays a major role against the dissolution of the material in the electrolyte, the formation of an oxide layer that hinders the passage of carriers, and/or against photocorrosion (see chapter 2.5).

Finally, low-cost materials are preferred because of the need of producing scalable devices.

2.6.2 PEC Configurations
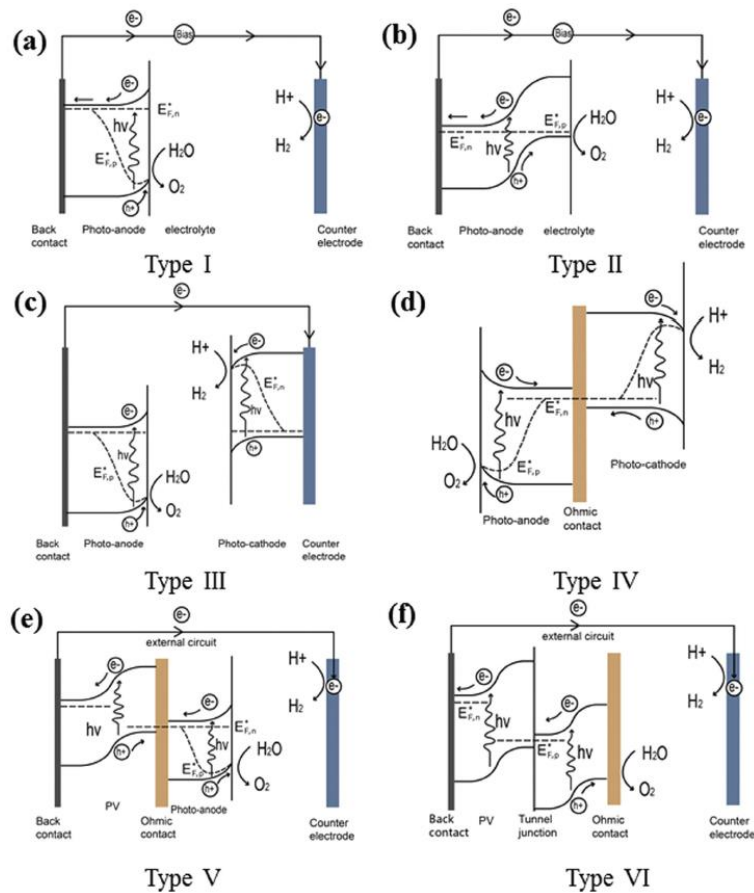
Figure 8. PEC Configurations. [21]

The configurations for the PEC devices are summarized in Figure 8. First type (a) contains a single light absorbing semiconductor and is normally the one used when the operation of these devices is being described. The semiconductor material can be used as a photoanode or photocathode to carry out oxidation or reduction of water. Normally, it consists of an n-type semiconductor as a photo anode and a metallic cathode separated by the electrolyte. $SrTiO_3$ (Egap of 3.2 eV) and $KTaO_3$ (3.5 eV) are used as photoanodes for PEC water splitting cells, with the aid of external bias. However, their large bandgap generates that only the UV portion of solar energy can be absorbed. Theoretical maximum STH efficiency limited to less than 1% is a consequence of this device limitation. [21]

Upon absorption of light, photoelectrons and holes are generated in CB and VB respectively. Due to the bending of the band formed at the interface, the holes move to the electrolyte to oxidize the water. Electrons are collected by a metallic substrate or by the transparent conductive glass (FTO glass or $F:SnO2$), withdrawn to the external circuit, pump up by a polarization potential, and come to the metallic cathode reducing water for the H_2 evolution. [22]

Two or more semiconductors are normally used to increase absorption and thus the number of charges that can be separated. Heterojunction is illustrated in configuration b, in these systems, light absorption and charge separation are improved by connecting a secondary semiconductor in the primary absorber. In addition, there are Tandem configurations where the photoanode and photocathode are connected in series, it is possible to have a wire connection (Configuration C) in which a conductive metal is used, or on the other hand, you can have a wireless connection in which a transparent conductive substrate is used for the electron and hole recombination layer.

Tandem cells increased the photovoltage but also de flexibility in materials selection because they minimize or eliminates the basic requirement of band edge potentials seen in a single semiconductor configuration, also, can have smaller bandgap and so increasing the light absorbability because each semiconductor need to provide only a half reaction. However, there exist two main requirements, the photoanode CB minimum must lie at lower or similar potentials than the VB maximum of the photocathode and both sides must maintain a similar current density when no external bias is applied.

In configuration e, there is the coupling with a PV cell that applies the additional bias. Wide bandgap materials are preferred for the front photoelectrode to enable adequate transmittance for further light harvesting by the PV [21]. When solar energy passes through the front PEC electrode and then reaches the rear PV device, the electrons or holes generated by the PEC electrode is recombined with the energy of the PV component and the remaining one is contributing to half of the reaction. The remaining charge of the PV device is then transferred to the counter electrode for the other half reaction of water splitting. [23].

Finally, PEC devices are facing three main challenges for increase the conversion efficiency: (i) Direct absorber band alignment is required to have the enough potential for both half reactions, having the proper position of Ec and Ev with respect to OER and HER. (ii) The wide bandgap is not optimized for the solar spectrum. (iii) Poor catalytic performance of the absorbers. These weak points can be solved using a buried-junction photovoltaic (PV) device and an electrochemical catalyst (EC) system, forming a PV–EC tandem (Configuration f). In a buried-junction device, the electric field is generated at an internal junction within the semiconductor and using ohmic contacts is then coupled with water splitting catalysts. The advantage is that it separates light absorption from catalysis and does not require the absorber to be stable in aqueous electrolytes in which the pH regime for the absorber and best water splitting catalyst may not be compatible. [24]

2.6.3 Key efficiencies for PEC devices

The overall solar to hydrogen (STH) efficiency is the most important measurement to characterize a PEC device. However, there are another important diagnostic efficiencies to understand the material performance: applied bias photon to-current efficiency (ABPE), external quantum efficiency (EQE), incident photon to current efficiency (IPCE), and internal quantum efficiency (IQE), absorbed photon to current efficiency (APCE). [23]

STH is defined as chemical energy produced divided by solar energy input. The numerator is the rate of hydrogen production multiplied by the change in Gibbs free energy per mol of H_2 (at 25°C, ΔG = 237 kJ/mol). The denominator is the incident illumination power density P_{total} multiplied by the illuminated area.

$$STH = \frac{(mmol\ H_2/s) * 237kJ/mol}{P_{total}(mW/cm^2) * area(cm^2)}$$

It describes the overall efficiency of a PEC device exposed to solar Air Mass (AM) of 1.5 illumination under zero bias applied. For a correct measurement the WE and the CE should be immersed in the same pH to avoid Nernstian bias that can arise from the chemical bias between the two solutions. Additionally, the electrolyte should not contain any sacrificial donors or acceptors because the redox reactions would no longer reflect true water splitting. There is an alternative way of calculating the STH since power can be expressed as the multiplication of the current, voltage and the faradic efficiency for hydrogen evolution.

$$STH = \frac{j_{SC}(mA/cm^2) * 1{,}23V * \eta_F}{P_{total}(mW/cm^2)}$$

Sometimes the application of a bias is needed and in that case the STH is not enough and can give an overestimation. The applied bias photon to current efficiency expresses the efficiency under the application of an additional voltage V_b as:

$$ABPE: \frac{j_{ph}(mA/cm^2) * [1{,}23 - V_b](V)}{P_{total}(mW/cm^2)}$$

In the ABPE the current j_{ph} is the photocurrent density obtained under an applied bias V_b.

Another important parameter is the photocurrent collected per incident photon flux as a function of illumination wavelength (IPCE). It reflects the combination of three processes efficiencies, (i) photon absorption defined as the fraction of electron-hole

pairs generated per incident photon flux, (ii) charge transport to the interface, and (iii) the efficiency of interfacial charge transfer. The last one in PV is often equal to 1 because charges are extracted to a metal forming the ohmic contact, but in PEC the interfacial charge transfer kinetics are often sluggish giving rise to a value less than 1. IPCE in a PEC system is measured by a chronoamperometry (potentiostatic) measurement and is normally calculated as:

$$IPCE\ (\lambda) = \ EQE\ (\lambda) = \eta_{e^-/h^+ generation} * \eta_{transport} * \eta_{interface}$$

$$IPCE\ (\lambda) = \ EQE(\lambda) = \frac{electrons/cm^2/s}{photons/cm^2/s} = \frac{j_{ph}(mA/cm^2) * 1239{,}8(V * nm)}{P_{mono}(mW/cm^2) * \lambda(nm)}$$

1239,8 V*nm represents the multiplication of the Planck's constant and the speed of light. P_{mono} is the monochromatic illumination power intensity, and λ is the illumination wavelength.

Finally, absorbed photon to current efficiency or internal quantum efficiency is the EQE but taking out the losses of impinged photons that are reflected or transmitted. In other words, is the photocurrent collected per incident photon absorbed.

$$APCE\ (\lambda) = \ IQE(\lambda) = \frac{EQE\ (\lambda)}{\eta_{e^-/h^+ generation}} = \eta_{transport} * \eta_{interface}$$

$\eta_{e^-/h^+ generation}$ is the absorbance and can be found using the Beer's law [25]. The absorbance (A) of a sample is the logarithmic ratio of the measured output light intensity (I) versus the initial input light intensity (I_0).

$$A = -\log\left(\frac{I}{I_0}\right)$$

$$APCE\ (\lambda\ ) =\ IQE(\lambda) = \frac{j_{ph}(mA/cm^2) * 1239,8(V * nm)}{P_{mono}(mW/cm^2) * \lambda(nm) * [1 - 10^{-A}]}$$

2.6.4 Chemical degradation and corrosion

PEC can experience photo corrosion. It is the mechanism of anodic and cathodic decomposition of semiconductor by bond breaking due to an accumulation of holes or electrons at the interface. Depends on the competition of charge transfer rates between the redox reaction and the corrosion process. Most of the semiconductor's materials that satisfy the energetic requirements of PEC are found to be susceptible to this type of corrosion.

At the anode usually all reaction products are soluble in the electrolyte and therefore the reaction can go on continuously. On the contrary, at the cathode there is the formation of an insoluble product left on the surface which quickly blocks the decomposition [magagnin]. The decomposition reactions are electrochemical reactions associated to an electrochemical potential called the decomposition potential.

Most of SC have their decomposition potential in the band gap of the SC on the energy scale. Meaning that for n-type, the holes at the VB can oxidize the SC in addition of oxidizing a redox couple lying in the band gap. In this case, for n-type the redox couple should lie negative of the decomposition potential to give electrode stability. In the case of p-type, SC's dark anodic decomposition reactions are expected due to the presence of excess holes at positive potentials respect flat band potential. [26]

$$E_{O_2/H_2O} < F_{dec,p} \qquad E_{H^+/H_2} > F_{dec,n}$$
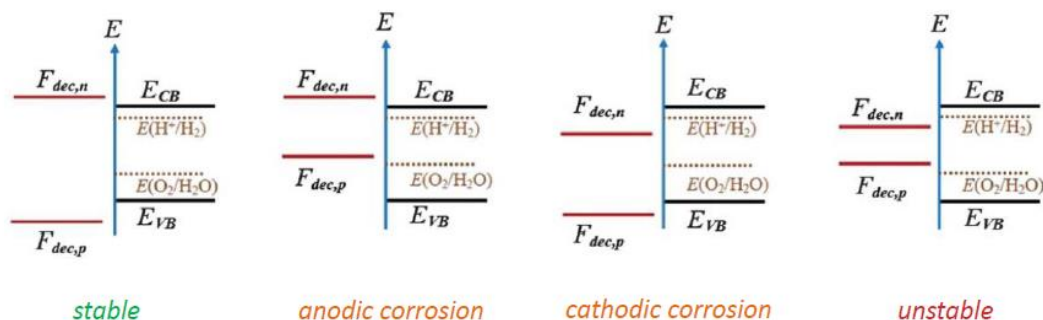
Figure 9. Effects in corrosion depending on the decomposition potential and redox couple potentials based on Gerischer and Bard criteria. [8]

Corrosion can be reduced by increasing the water splitting kinetics, avoiding charge accumulation. Moreover, oxides or conductive polymer like polyaniline coatings with higher resistance also in acid electrolytes are employed, as well as nanoparticles and fusible alloys are employed too. Another approach consists of using another semiconductor more resistant to photocorrosion as a thin layer (TiO_2) but it must have a proper alignment of the band edges to not increase the charge transfer resistance [27], the anodic deposition potentials of TiO_2 and Fe_2O_3 are above the VB potential, but they are thermodynamically stable because of their very slow decomposition reaction kinetics. [21]

2.7   Materials for PEC device

Semiconductor materials for PEC photoelectrodes can be classified in poly-crystalline and single-crystalline. The former includes metal oxides, nitrides, oxynitride and so on. For example, TiO_2, a-Fe_2O_3, $BiVO4$, WO_3, and ZnO are used as photoanodes, while Cu_2O, $CuFeO_2$ and $CuInS_2$ are used as photocathodes. One the other hand, the singlecrystalline semiconductors includes Si and III–V materials (for example, GaAs, InP, GaN and GaP) that are used in both cases. Some materials used as photocathodes and photoanodes will be described in this Chapter.

2.7.1 Photocathode materials

2.7.1.1 Cu₂O

Cuprous oxide have an Egap of 2eV and its CB position is suitable for light-driven hydrogen evolution from water. The advantages of using this material are the scalability, low toxicity, abundance and high theoretical photocurrent of 15 mA/cm², together with a potential 18% STH efficiency under AM 1.5G. However, the problem is that the redox potentials for the reduction and oxidation of monovalent copper oxide lie within the band gap, affecting the stability [28]. Solutions for this problem can be in first place, the combination with a more positive conduction band material (n-type semiconductor), promoting the fast transfer of photoelectrons from Cu2O to the n-type semiconductor through the formation of a p-n junction.

Secondly, the deposition of a thin film made of carbon or metal oxide. Configurations such as Cu₂O/ZnO/Al₂O₃/TiO₂/Pt, Cu₂O nanowire/AZO/TiO₂/RuOx and Cu₂O/AZO/TiO₂/MoS₂ have been reported, but their high cost and limited long-term stability hamper their use in practical devices. [28]
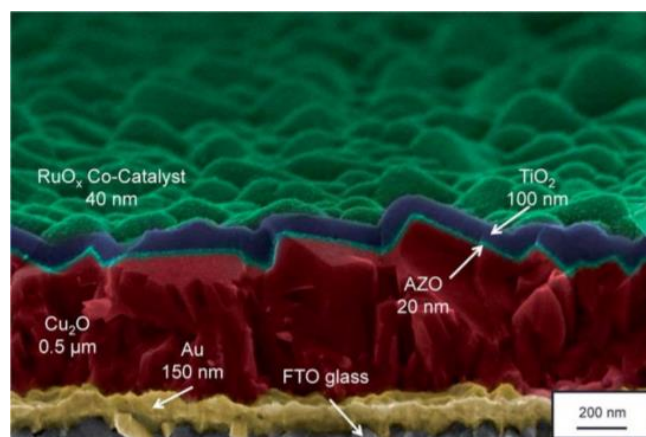
Figure 10. Cross-sectional SEM image of a photocathode with respective ALD layer thicknesses. [28]

CuO can also be used and CuO nanowire-based photocathodes (Figure 11) exhibit an onset potential at ~700 mV vs. RHE. The CuO photocathode shows a photocurrent of ~1.4 mA cm⁻² at 0 V vs. RHE under AM 1.5 G, which is one of the highest photocurrents based on bare CuO photocathode. The problems of stability are minimized depositing cocatalyst by galvanostatic photodeposition, RuOx and/or Pt

nanoparticles on the CuO nanowires surface, accelerating surface reaction and inhibiting the charge accumulation at semiconductor/solution interface [29].
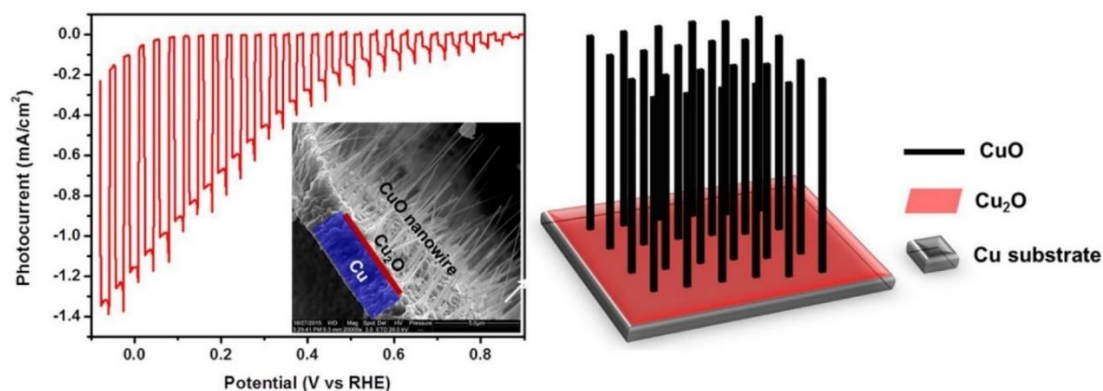
Figure 11. (left) I-V characteristic curve for CuO photocathode, and morphology of a Cu/Cu₂O/CuO photocathode. (right) Structure scheme of Cu/Cu2O/CuO photocathode prepared via thermal processes. [29].

2.7.1.2 CIGS

Cu(In,Ga)Se₂ (CIGS) is a scalable candidate of photocathode material, others advantages are listed below:

- Tunable Egap over the range of 1.0–1.7 eV by Ga/In ratio.

- Good photoabsorber with a record solar cell efficiency of 20.4%.

- It can be produced with reasonably low cost by industrialized processes.

- CB edge that is well positioned for the hydrogen evolution half-reaction.

CIGS has a narrow band gap of 1.2eV, being very close to that of the Si. However, its CB energy is quite deep, lying at −0.2 V vs RHE, that offers only moderate driving force for the H₂ evolution reaction [30]. Thus, the use of Pt as catalyst is mandatory.

An outstanding photocathode generating a photocurrent density of 25 mA/cm² using CIGS/CdS/Pt at applied potential of 0V versus RHE under standard 1 sun illumination and in a neutral pH electrolyte was reported. Surface modification with thin conductor layers composed of Mo and/or Ti and high degree of contact between the Pt particles

and the Mo/Ti layer can improve the stability [30]. However, the scarcity of In element is a real problem in the construction of large scale PEC devices.

2.7.1.3 Group III–V metal phosphides

GaP has an indirect Egap of 2.26 eV, with a CB located at 0.6 V vs. NHE at pH = 0, and InP exhibits a band-gap of 1.35 eV, representing near-optimal absorptivity of the solar spectrum. These materials could be used for photocatalytic water reduction to produce H_2, but the problem again is the photocorrosion. Amorphous TiO_2 has been employed as a surface passivation layer and the large VB offset between TiO_2 and these metals phospides can create an energy barrier for holes reaching the surface, reducing the recombination.

Gallium indium phosphide ($Ga_{0.51}In_{0.49}P$, referred to as $GaInP_2$), is an indispensable materials component for realizing high STH efficiency (>20%) due to its near ideal Egap of ~1.8 eV for the large Egap material in multijunction photoelectrode [31]. Hannappel and co-workers have developed a tandem structure consisting of a GaInP n–p top cell (Egap of 1.78 eV) and GaInAs n–i–p bottom cell (Egap of 1.26 eV) with Rh electrocatalysts deposited onto the surface. The as-prepared tandem device yields an STH of 14% and 17% for unbiased and potentiostatically assisted water splitting [32].

2.7.1.4 Silicon

Silicon with an Egap of 1.11 eV is the most successful material in PV and microelectronics industries, its Egap is relatively well matched to the solar spectrum and its theoretical maximum photocurrent can reach up to 44 mA/cm2 under AM1.5 G one Sun illumination [33]. These properties render Si a promising material for photoelectrodes in a PEC water splitting system. Nonetheless, using Si as a photoelectrode in PEC devices have some problems to be solved. First, a large proportion of incident visible light are reflected on a planar Si/water interface. Secondly, the corrosion, and finally, the sluggish water splitting kinetics on Si surfaces.

To solve these problems, we can increase the surface textures on planar Si surface, strengthening light absorption and exhibiting the best competitiveness due to the omnidirectional broadband light trapping and relatively low surface recombination.

Moreover, this texture will increase the adhesion allowing the deposition of a conformal thin protecting layer improving the stability of the photocathode. Also, the use of effective catalyst like Pt, Ru and Ir oxides is important, but they are too expensive for commercial use. For this reason, metal-based alloys such as NiMo and NiFe exhibit comparable and even higher PEC activity. Finally, a rear p^+ emitter on n-Si photocathode allows light illumination from the rear side of the device, which spatially and functionally decouples the optical absorption and the catalytic activity of the photocathode. The highest reported efficiency for a Si photocathode up to now is 11.5%. [33]
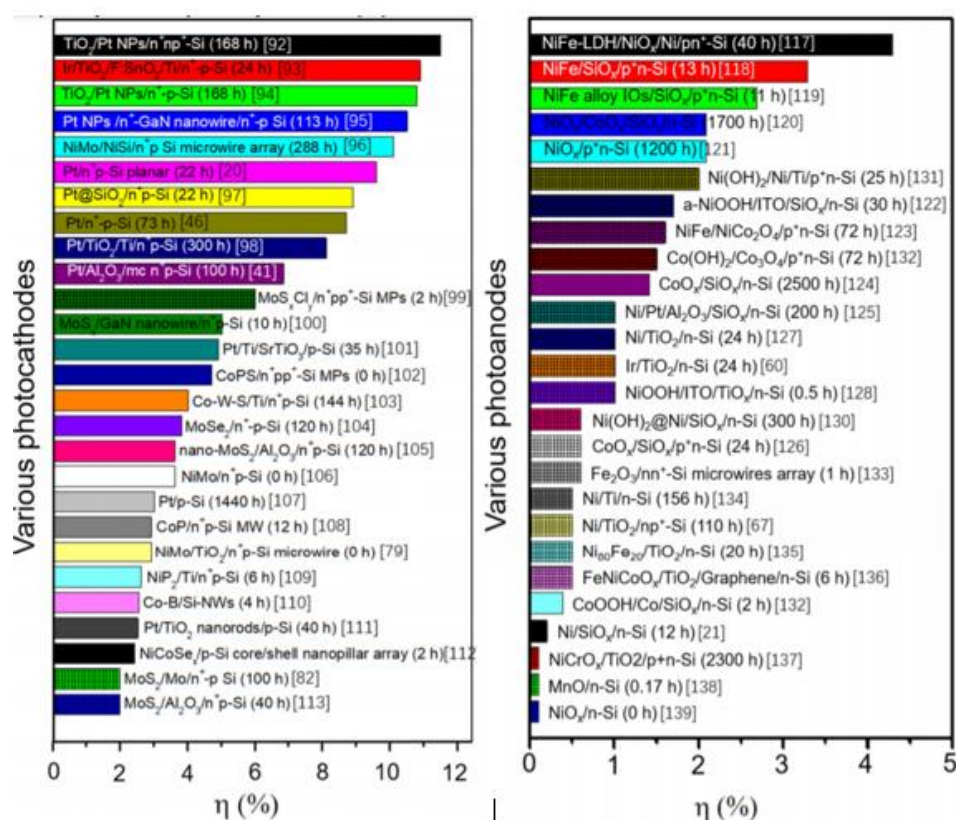
Figure 12. Chart visualizing data on reported η of various Si photocathodes for HER and Si photoanodes for OER. [33]

2.7.2 Photoanode materials

2.7.2.1 TiO₂

TiO₂ based photoanodes are composed of earth-abundant, nontoxic elements and are photochemically stable under either strongly acidic or strongly basic conditions.

However, the wide Egap of 3.2eV leads to an absorption only of 5% of the solar spectrum (predominantly UV light), which result in a very low maximum theoretical STH efficiency (η = 1.3% for anatase and 2.2% for rutile TiO2).

The Egap can be modified by changing the VB introducing non-metal species, such as carbon or nitrogen, through forming mid-gap states, or modifying the CB by forming donor states below it by doping with 3d transition metal ions. However, the efforts up to know have not produced a big change and although doping can extend the light absorption to the visible range, the optical absorption is still very moderate above 450 nm. By introducing a dopant through the hydrogenation of TiO_2 nanocrystals, it is possible to synthesise a disordered TiO_2 nanophase of black colour, corresponding to a band-gap energy of 1.0 eV. [34]

Another issue is the high density of bandgap trap states resulting in fast charge carrier recombination and poor electrical conductivity. The aim is to create oxygen vacancy in TiO_2 to modify the electronic and optical properties, this can be achieved by thermal annealing, electrochemical reduction, hydrogen treatment, flame reduction and chemical reduction [35].

The performance of TiO_2 improve with the Pt-coated TiO_2 nanorods because the last enhance the photoactivity in the uv-visible region compared to the TiO_2, and photocurrent is dominated by the photoactivity of TiO_2 in the UV region, thus, improving the photocurrent 1.86 times from 0.36 mA/cm^2 to 0.67 mA/cm^2 [36].

2.7.2.2 α-Fe$_2$O$_3$

Hematite is a natural abundant compound with good chemical stability, low toxicity, and low cost. In addition, it has a Egap value between 1.9 and 2.32 eV, allowing for visible light absorption up to 40%. However, the CB position is significantly more positive than the proton reduction potential and thus can only be used for PEC water oxidation with an external bias. Other problems are its sluggish oxygen evolution kinetics at photoanode/electrolyte interfaces, poor bulk charge transport that leads to short hole-diffusion length, slow OER kinetics, and high electron–hole recombination rate.

Interfacial engineering at photoanode/electrolyte is used to address high electrical potentials because photogenerated holes need to be transfered from the hematite surface to the electrolyte. This can be achieved by passivating the surface defect sites becuase it provides provides a favorable pathway for better holes extracting from its VB. Also, by using OER catalysts decreasing the activation energy (Figure 13), and finally, using surface treatments that will activate the surface and remove the defects improving the stability [37]. This activation is performed reducing the hematite surface defects, making richer Nb-O and Sn-O bonds, and generating more Fe2+ ions or oxygen vacancies in hematite bulk [38].
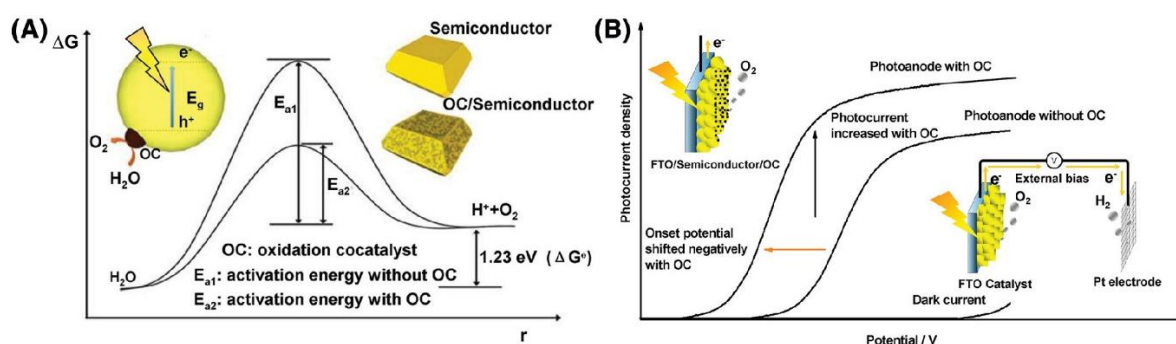
Figure 13. Schematic description of the role of oxidation cocatalyst in (A) photocatalytic water oxidation and (B) PEC water oxidation. [39]

Photoanode/substrate interface engineering can be implemented by inserting a conductive underlayers between FTO and hematite, thus, reducing the recombination sites especially for very thin film of hematite. Finally, interface engineering inside photoanodes by nano-structuring, heterojunctions, and engineering at grain boundaries are useful to change the poor carriers transport and separation.

The performance of hematite-based photoanodes have improved in the recent years reaching photocurrents of 6.0 mA/cm^2 at 1.23 V$_{RHE}$ with stability over 100h but the need of achieving the maximum theoretical photocurrent delivered by hematite ($\sim$12.6 mA cm^{-2}), low onset potential ($\sim$0.4 V$_{RHE}$), long-time stability (>100 h), and large-area is still present and under research. [37]

2.7.2.3 BiVO₄

Photoelectrochemical properties of $BiVO_4$ are strongly dependent on its crystalline structure. The highest activity towards water oxidation was reported for the monoclinic scheelite structure, in which better properties with respect to the tetragonal zircon-type one appears to be mainly due to the enhanced photon absorption, caused in turn by an Egap value of 2.4 eV, sensibly lower than the 2.9 eV of zircon-type structures.

The maximum theoretical photocurrent is 7.4 mA/cm² at 1.23 V vs. RHE and the maximum theoretical STH efficiency is 9.1%. The latter is limited by fast charge carrier recombination due to its only 10nm electron diffusion length and the material also exhibits poor surface water oxidation kinetics. However, the electron diffusion length can be increased up to 300nm doping with Mo and W. The poor surface reaction kinetics can be improved by the addition of oxygen evolution co-catalysts such as Co–Pi (cobalt phosphate). [21]

Some of the most important characteristics that make $BiVO_4$ stand out among other metal oxides for PEC applications are [30]:

- A 2.4 eV Egap value of the monoclinic scheelite structure corresponding to the 520nm absorption of radiations, allowing good absorbance in the visible range.

- A sufficiently negative VB edge position (2.4 V vs RHE) with respect to water's oxidation potential, providing a high enough overpotential for holes to oxidize H_2O at the anode.

- CB level around 0 V vs RHE, having a thermodynamic level close to H2.

- The electrons and holes effective masses are lower than in similar semiconductors (like In2O3 or TiO2), resulting in easier separation and extraction processes for charged species.

- non-toxicity of the material.

- inexpensiveness of the elements in the compound.

The biggest disadvantage is the surface, characterized by inefficient water oxidation kinetics, poor charge transport properties and high frequency of electron-hole recombination events. To overcome these problems doping is used, nanostructuring and control of the morphology, formation of composite structures and superficial application of photocatalysts are other alternatives.

Mayer[40] found that $BiVO_4$ exhibited the highest photovoltage (≈ 1.0 V) among common visible-light active-metal oxides (Fe_2O_3, $ZnFe_2O_4$, Cu_2O, and WO_3) and showed the best performance among photoelectrodes working in direct contact with the electrolyte. Solution-based metal organic deposition (MOD) and thermal conversion are the most frequently used synthesis methods. The MOD yields $BiVO_4$ with high nanoporosity and it is highly compatible with heterojunctions and doping, it easily produces $BiVO_4$ photoanodes showing photocurrents above 5.0 mA/cm^2 at 1.23 VRHE under 1 Sun irradiation. The best planar $BiVO_4$ without electron transport layer fabricated by laser evaporation-driven, facet-engineered $BiVO_4$ achieved 6.1 mA/cm^2 at 1.23 VRHE with Co–Pi and surface etching [41]. 6.7 mA/cm^2 at 1.23 VRHE was achieved with a Co–Pi/$BiVO_4$/WO_3 nanowire prepared by glancing angle deposition (GLAD) on ITO/Pt/ITO. Figure 14 shows the $BiVO_4$ performance as light absorber and forming a heterojunction. The 2.4–2.5 eV indirect Egap cannot realize η_{STH} above 10%, and further improvement must be achieved by combination with smaller bandgap light absorber, like Fe_2O_3, or from extending the light utilization to longer wavelength photons by Egap engineering.
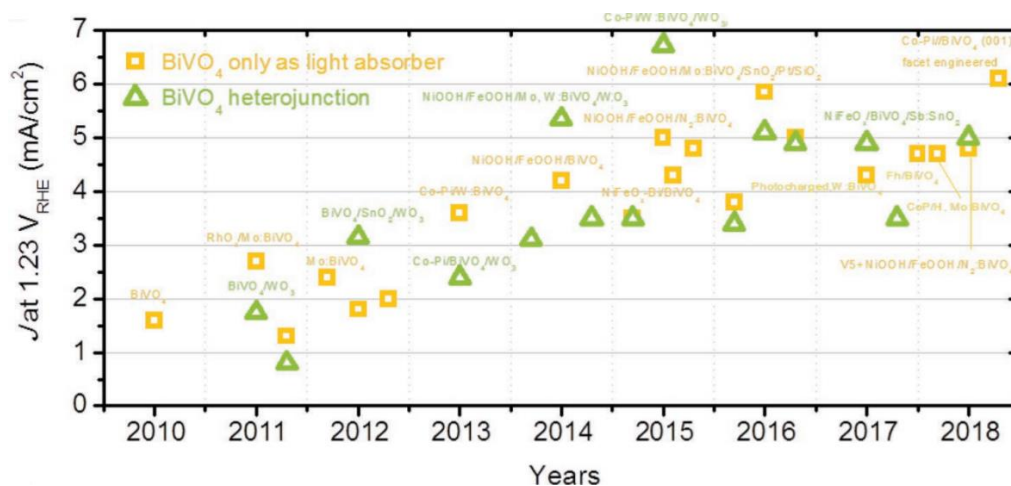
Figure 14. $BiVO_4$ based photoanodes performances at 1.23 VRHE and under simulated 1.0 Sun condition (100 mW/cm^2) working as light absorber and heterojunction. [41]

2.7.2.4 CdS

CdS has a narrow Egap of 2.4eV and CB situated at -0.7V while the VB is at 1.7V NHE (pH=0), so, in theory, H_2 and O_2 oxidations under visible light are feasible with pure CdS. The problem is the severe anodic corrosion due to the poor water oxidation kinetics that generates the accumulation of holes at the surface. Scavengers like SO_3^{-2} are used to mitigate these effects. Also, surface passivation layers are used to increase the reaction kinetics and protect the semiconductor from corrosion. Situation also needed for other II-VI elements like CdTe, CdSe, ZnTe [21].

There are methods reporting a two-step hydrothermal method to synthesize nano step CdS (straight rod as the backbone and a nano step-structured morphology on the surface) as photoelectrodes for improved PEC performance. (Figure 15)
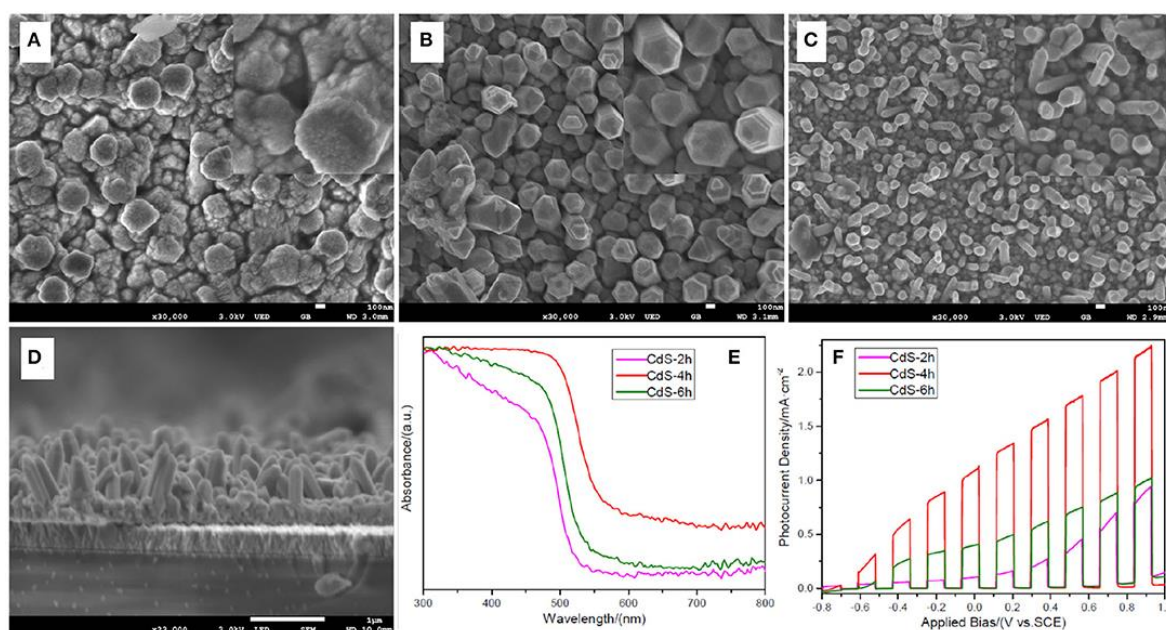
Figure 15. SEM) images of (A) sample CdS-2h; (B) CdS-4h; (C) CdS-6h; (D) cross-section of CdS-4h; (E) Uv-Vis absorbance of CdS-2h, CdS-4h, and CdS-6h; (F) linear sweep voltammetry (LSV) curves under chopped light illumination. [42]

It is possible to reach a value of 1.88 mA/cm² at 1.23V RHE or 0.576V SCE [42]. This can be improved by a immersing during 30s the CdS-4h in 3.7wt% HCl solution before a second hydrothermal process is applied. Then, this sample is placed in an autoclave containing the same precursor at 200°C for 3 h and now it is named CdS-HT-3h. The results are shown in figure 16. [42]
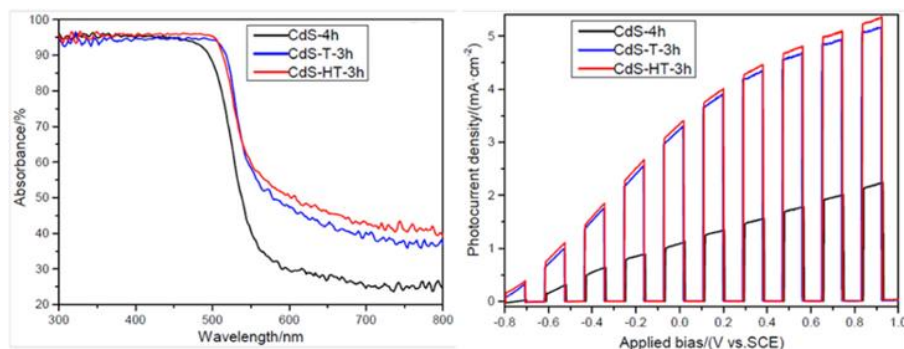
Figure 16. Comparison between the absorbance and the LSV of the CdS-4h, CdS-T-3h, and CdS-HT-3h. [42]

In figure 13 it is observed that the photocurrent density is almost 2.7 times times of the CdS-4h reaching up to 5 mA/cm^2.

2.7.3 CZTS

As it was stated above, the scarcity of In element is a real problem in the construction of large scale PEC devices. In this context, there is the need of search for potential alternatives to these chalcopyrite-type materials. Although, the current record of such a chalcogenide-based photocathode is 32.5 mA cm^{-2} at 0 VRHE using a CIGSe/CdS/ZnO stack, the CIGSe was fabricated using vacuum coevaporation, which is costly and may be challenging for large-scale application [43]. An attractive example is Cu_2ZnSnS_4 (CZTS), a p-type quaternary semiconductor compound with the kesterite crystal structure which has a direct Egap of 1.5 eV and CB edge potential of −0.7 V vs. RHE. The advantages are that CZTS is composed of abundant elements in the earth`s crust, fair absorption properties, and environmental friendliness that serves as a suitable photocathode candidate. However, its performance is limited by poor bulk and surface transport properties.

The first application of CZTS as a photocathode achieved a photocurrent of 9 mA/cm^2 [44]. After that, using a similar photocathode stack of solution-processed CZTS/CdS/TiO$_2$/Pt illustrated in figure 17, the highest photocurrent was, as shown in figure 18, 11 mA cm^{-2} at 0 VRHE [45]. This difference in performance between CZTS and CIGS, despite their similar optical properties, presents an opportunity to improve the stack and the bulk properties of CZTS.

The limitation in performance of CZTS solar cells is due to the large concentration of CuZn antisites that form defect clusters and the formation of detrimental secondary phases such as ZnS and Cu_2S [46]. To improve the performance of CZTS, doping operations must be performed. This will be explained in the next section.
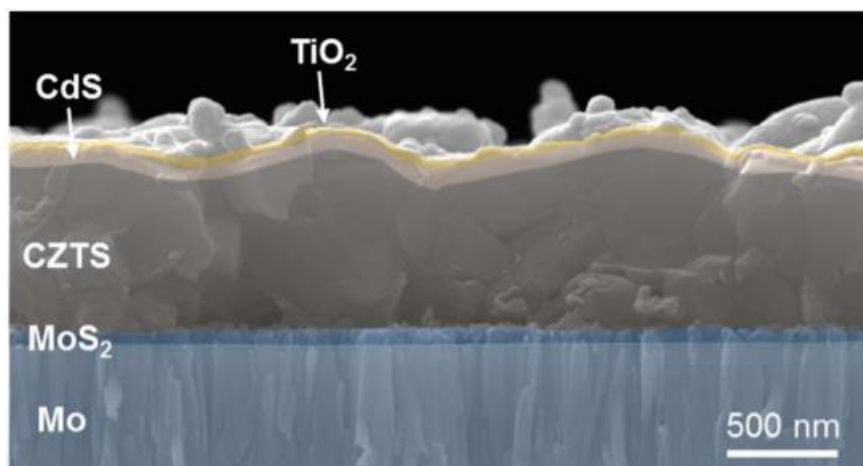
Figure 17. Cross-sectional SEM image of a CZTS/CdS/TiO$_2$/Pt photocathode. [45]
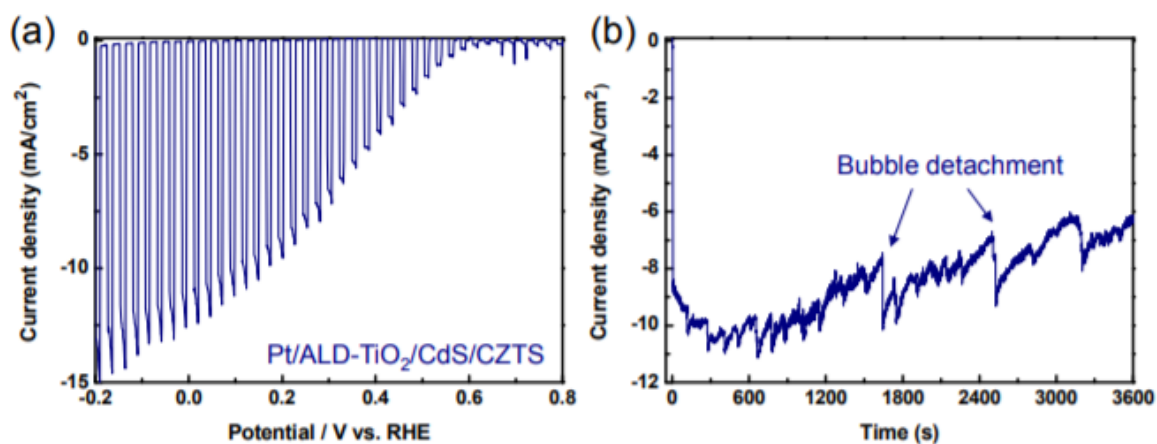
Figure 18. (a). Current density-potential curves of a CZTS/CdS/TiO$_2$/Pt photocathode in a phosphate-buffered aqueous solution at pH 6.85 under chopped solar-simulated light illumination (AM 1.5G) and (b) the corresponding current density-time curve with an applied bias of 0 V vs. RHE. [45]

2.8 Doping of CZTS

To improve the defect characteristics of CZTS, cation substitution is employed. Specifically, cations in CZTS are replaced by other isovalent elements preventing the

formation of antisite defects. For example, Cu+ can be replaced by Ag+, and Zn^{+2} can be substituted by Ba^{+2} or Cd^{+2} [47].

2.8.1 Self-doped CZTS

A series of self-doped CZTS nanocrystal (NC) films with Sn ions partially replaced by Zn ions were prepared from their colloidal solutions, depositing Zn on a fluorine doped tin oxide (FTO) glass substrate by electrophoretic deposition. Seeing the figure 19, the Raman peaks of the self-doped CZTS samples showed gradual shifts toward higher wavenumbers.
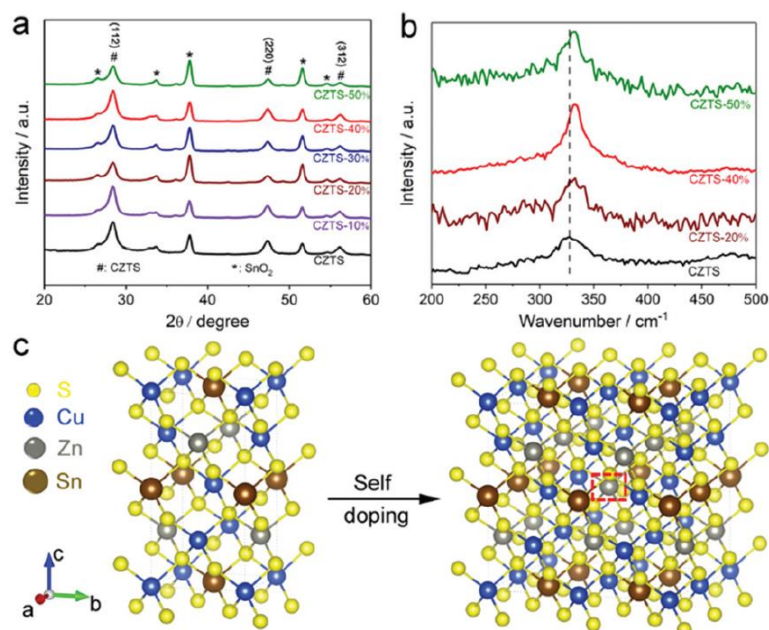
Figure 19. (a) XRD patterns, and (b) Raman spectra of CZTS and self-doped CZTS. (c) The schematic supercell of CZTS and self-doped CZTS. The red dash rectangle shows the self-doping site.[47]

The difference in the reaction rate of Zn and Sn precursors with sulphur generates that the particle size decreased with the increase in the doping ratio. Also, Increasing the self-doping ratio change the Egap from 1.50 to 1.55 eV. The current–potential curves of CZTS and self-doped CZTS NC films are shown in figure 20.
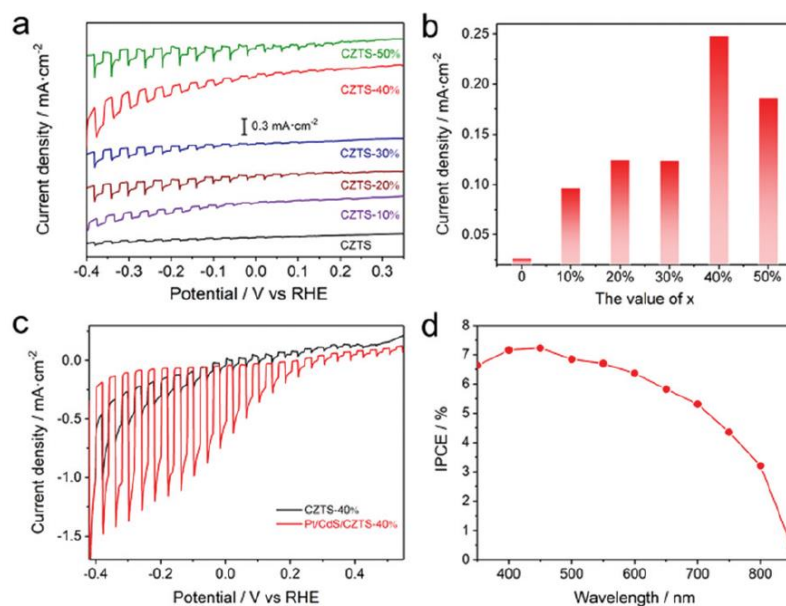
Figure 20. (a) Current density–potential curves of the CZTS-x photocathodes with varied x values. (b) Photocurrent density of CZTS-x photocathodes measured at an applied potential of -0.3 V vs. RHE. (c) Current density–potential curves of CZTS-40% and Pt/CdS/CZTS-40% photocathodes. (d) IPCE measurement of the Pt/CdS/CZTS-40% photocathode at an applied potential of 0 V vs. RHE.[47]

First, in figure 20(a) is clear that all the samples exhibit negative photocurrents meaning that the material is a p-type, so it works as a photocathode for hydrogen production. Self-doped CZTS films showed improved PEC performances compared to the pristine film. The best PEC performance gives a photocurrent density of -0.25 mA cm^{-2} at -0.3 V vs. RHE using CZTS-40% photocathode but if it is improved with CdS and Pt, a photocurrent density of 1.2 mA cm^{-2} is achieved. Furthermore, it was found that the VB minimum and the CB maximum of the self-doped CZTS both showed an upper shift compared with those of CZTS, the defects in CZTS can induce a deep trap state within the Egap that works as a recombination centre (Figure 21). This is not the case of the CZTS NC self doped where a shallow defect level forms, increasing the carrier density and improving the carrier mobility.
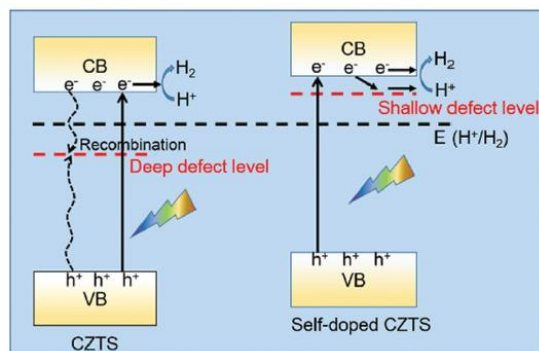
Figure 21. Schematic of the proposed mechanism for the charge transfer in CZTS and self-doped CZTS. [47]

2.8.2 Si-Doping of CZTS

The density functional theory calculations show that increasing Si yields an Egap rise due to shifting of the CB minimum towards higher energy states in the $Cu_2Zn(Sn_{1-x}Si_x)S_4$, Si doping inverts the band bending at grain boundaries (GB) from downward to upward and the fermi level of the new compound CZTSiS shifts upward. The Si doping arises from the idea that Sn is volatile at T>400°C, temperature achieved during the sulfurization process. The problems are that SnS_2 will form a secondary diode, and the formation of SnS secondary phase will form an non desirable band alignment with CdS.

The Si substitution can be performed by sputtering method (RF of 70W for 5min) depositing a thin film of Si over the CZT layer. The CB minimum and the VB maximum are dominated by hybridization of the S-p and Sn-s orbitals and the Cu-3d and S-p hybridization respectively. Therefore, the modification in the density of states near the CB minimum where chemical environment changes from Sn to Si increase in the Egap of the material from 1.44eV to 1.47eV, and up to 1.86eV for pure $Cu_2ZnSn_xSi_{1-x}S_4$ [48], which is considered to be the ideal Egap for water splitting process. Tauc plots are shown on figure 22 d.
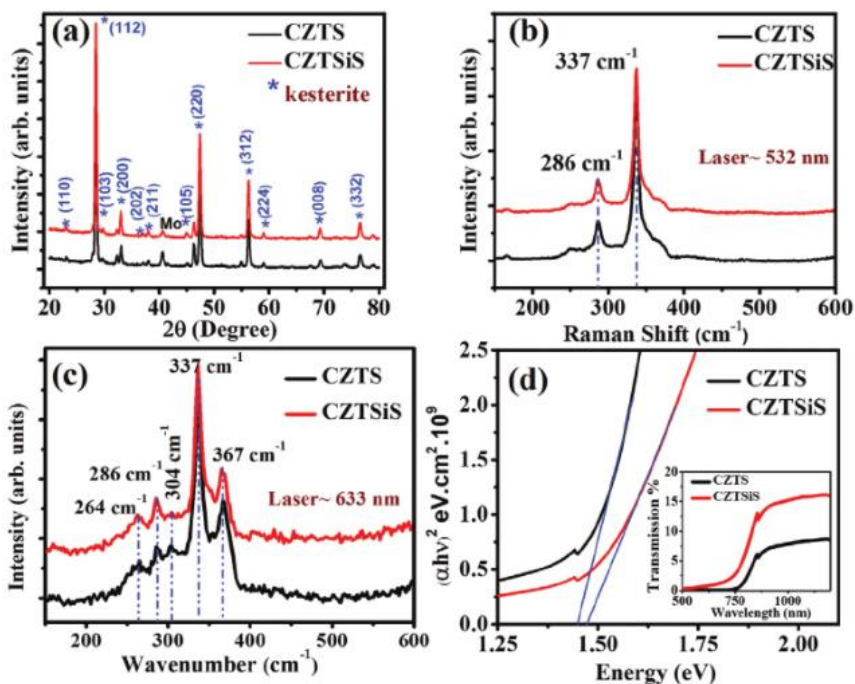
Figure 22. a) XRD spectra, and Raman spectra at b) 563nm, c) 633nm laser excitation sources, and d) Tauc plots of kesterite thin film samples.[48]

CdS was used as the buffer layer, followed by the protecting layer ZnO. The photocurrent density of the CZTS/CdS/ZnO electrode was 1.9 times higher that the pristine CZTS reaching 3.75 mA cm⁻² at −0.40 VRHE. The photocurrent density using CZTSiS with the same buffer and protecting layer reached 5.41 mAcm⁻² at −0.40 VRHE, which is 2.8 and 2.1 times higher than that of pure CZTS and CZTSiS, respectively [48]. Results are shown below in figure 23.
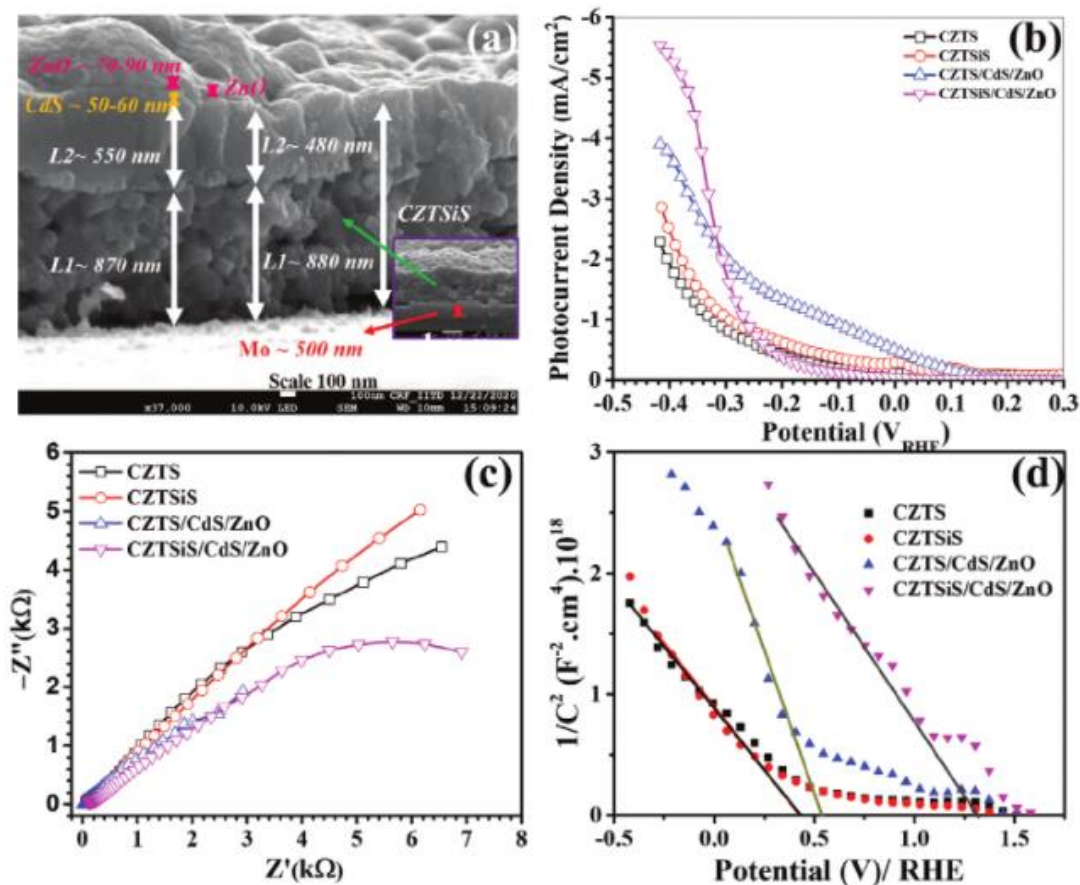
Figure 23. a) Cross-sectional image of CZTSiS/CdS/ZnO sample (ZnO is top layer), b) current density–potential curve, c) Nyquist plots, and d) Mott–Schottky plots of the CZTS, CZTSiS, CZTS/CdS/ZnO, and CZTSiS/CdS/ZnO photocathodes.[48]

2.8.3 Cd Doped CZTS

In this work, a photocathode design consisting of solution processed CuCdZnSn (CCZTS) photoabsorber coated with Pt is going to be studied. Basically, we replaced Zn with Cd partially to prepare a pure sulfide (CCZTS)-based photocathode via sol-gel method.

Cd substitution increases the grain size, suppresses formation of ZnS secondary phase, and reduces Cu/Zn antisites. Ying Fan Tay et al [49] performed Cd doping on CZTS improving the bulk quality and enhancing the photocurrent from 4 mA/cm² to 17 mA/cm² at 0VRHE, leading to an increase in EQE and an overall power conversion efficiency enhancement from 5.3% to 9.24% with 40% Cd doping. CZTS is a promising photoabsorber as a photocathode for water reduction to produce hydrogen, but its

performance is often limited by the presence of a high concentration of defects, large concentration of CuZn antisites that form defect clusters and the formation of detrimental secondary phases such as ZnS, SnS_x and Cu_2S. The objective is to integrate this solution on a transparent substrate producing a monolithic cell that will be analyzed in front and rear illumination.

3. Materials and methods

3.1 Preparation of CCZTS films

The precursor sol solution was prepared by dissolving $Cu(CH_3COO)_2 \cdot H_2O$ (0.38 mol L^{-1}), $Zn(CH_3COO)_2 \cdot 2H_2O$ + $Cd(CH_3COO)2 \cdot xH_2O$ (0.25 mol L^{-1}), $SnCl_2 \cdot 2H_2O$ (0.2 mol L^{-1}), and $SC(NH_2)_2$ (0.8 mol L^{-1}) into 2-methoxyethanol. Adjusting Cd and Zn relative quantities so that Cd/(Zn+Cd) = 0.4. Then, stirring in warm water bath at 50 °C for 2 h to get dark yellow solution.

The ratios of Cu/(Zn+ Cd + Sn) and (Zn + Cd)/Sn were 0.86 and 1.25 respectively in the precursor solutions, following a Cu-poor, Zn-rich composition. The selected FTO substrate was cleaned by sequential ultrasonication in 10 g/L ALCONOX detergent solution and ethanol. Then, the prepared sol solution was spin coated on FTO at 3000 rpm for 30 s followed by preheating at 200 °C for 2 min on a hot plate in air. The spin coating was repeated from 2 to 20 times to obtain the desired thickness (2,5, 10, 13, 15 and 20 layers).

Spin coating is a method to apply a uniform film onto a solid surface by using centrifugal force and requires a liquid–vapor interface. In a typical procedure, a liquid is placed at the center of a circular surface and is rapidly rotated to produce uniform films of 1–10µm in thickness. The substrate is firmly secured onto a rotating plate thanks to a vacuum pump connected to the instrumentation, and it starts rotating with increasing speed. Rotation at high speed is needed to produce centrifugal forces

allowing the liquid phase to spread evenly onto the substrate, with excessive fluid being spun of the plate's edges, until the desired film thickness is produced. The spin coater used was the Laurell ws-650 sz-8npp/lite.

Then, precursor films were subjected to sulfurization at 560°C in sulfur atmosphere to obtain CCZTS thin films. The sulfurization treatment was performed placing the precursor inside a graphite box of $20cm^3$ internal volume, with 150 mg of elemental sulfur and 15mg of metallic Sn powder. The furnace was heated at 15°C/min to 560 °C and maintained for 45 min in argon atmosphere. The films were cooled naturally in the furnace under sulfur atmosphere. The concentration of each metal ion is close with the generally reported data for high efficiency cells, thiourea was used to complex metal ions and to provide sulfur during the annealing process. Tin powder is introduced in the chamber to compensate tin loss from the precursor.

Detailed reaction equations are shown as follows:

$$M–X + Tu \rightarrow [M(Tu)_m]–X$$

$$[M(Tu)_m]–X + ROH \rightarrow [M(Tu)_m]–OR + H–X$$

$$[M(Tu)_m]–X + [M(Tu)_m]–OR \rightarrow [M(Tu)_m]–O–[M(Tu)_m] + R–X$$

$$[M(Tu)_m]–O–[M(Tu)_m] + R–X \rightarrow Cu_xS + ZnS + Sn_xS + SnO_2 + volatile\ matter$$

$$Cu_xS + ZnS + Sn_xS \rightarrow Cu_2ZnSnS_4$$

$$Cu_xS + ZnS + SnO_2 + S \rightarrow Cu_2ZnSnS_4$$
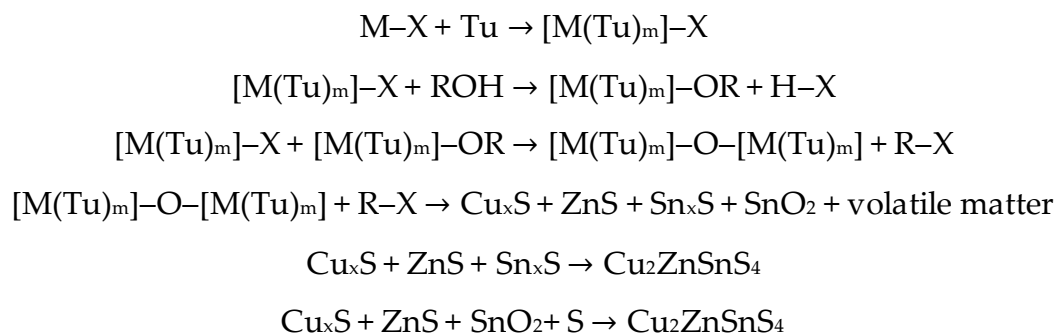
In these equations, the symbols (M, X, Tu and R) represent metal ions (Cu^{2+}, Zn^{2+}, Sn^{2+}), anions (CH_3COO^- or Cl^-), thiourea and organic molecular chains of 2-methoxyethanol, respectively.

3.2 Deposition of CdS

CdS was used as a buffer layer and it was deposited onto the absorber material by chemical bath deposition (CBD), a two steps method (nucleation and particle growth, and is based on the formation of a solid phase from a solution) to deposit thin films and nanomaterials that requires only solution containers and substrate mounting devices and yields adherent, uniform, stable and hard films with good reproducibility.

CBD for CdS requires cadmium acetate dihydrate ($Cd(CH_3COO)_2$) as precursor for the cation (Cd^{2+}), ammonium chloride (NH_4Cl) as complexing agent, thiourea ($SC(NH_2)_2$) was the precursor for sulfur, and ammonium hydroxide (NH_4OH) solution was added in order to have a basic pH. The complexing agent is used to slow down the process, while the basic pH is needed to hydrolyze thiourea and release sulfide ions.

Several reversible reactions are involved in the process. In case of the deposition of CdS they are:

$$Cd(CH_3COO)_{2(aq)} \leftrightarrow Cd^{+2}{}_{(aq)} + 2CH_3COO^-{}_{(aq)}$$

$$NH_4Cl_{(aq)} \leftrightarrow NH_4^+{}_{(aq)} + Cl^-{}_{(aq)}$$

$$NH_4^+{}_{(aq)} + OH^-{}_{(aq)} \leftrightarrow NH_{3(aq)} + H_2O_{(l)}$$

$$Cd^{+2}{}_{(aq)} + 4NH_{3(aq)} \leftrightarrow [Cd(NH_3)_4]^{+2}{}_{(aq)}$$

$$Cd^{+2}{}_{(aq)} + 2Cl^-{}_{(aq)} \leftrightarrow CdCl_{2(aq)}$$

$$SC(NH_2)_{2(aq)} + 2OH^-{}_{(aq)} \leftrightarrow S^{-2}{}_{(aq)} + CH_2N_{2(aq)} + 2H_2O_{(l)}$$

$$Cd^{+2}{}_{(aq)} + S^{-2}{}_{(aq)} \leftrightarrow CdS_{(s)}$$
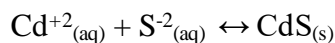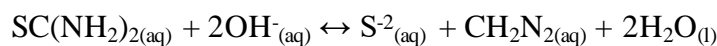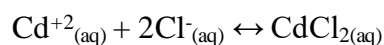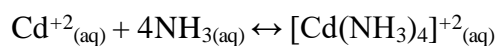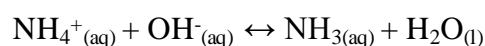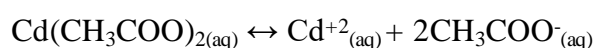
The growth of the buffer layer occurs by the direct deposition of the ions onto the surface of the sample and by the deposition of crystals formed in the liquid bulk. CdS gives rise to a yellow suspension, the intensity of the color of the mixture increases with time and the solution becomes less and less transparent.

The CBD of CdS was performed according to the following recipe. First, an aqueous solution of 216ml containing about 5.8 mM $Cd(CH_3COO)_2$, 44 mM NH_4Cl and 840 mM NH_4OH was prepared. The sample is put into the solution, which is then heated up to 75 °C and covered to limit the evaporation of water and ammonia. After the desired temperature has been reached, an aqueous solution of 35 ml containing 79 mM thiourea is added to the hot liquid causing a temperature drop of about 5 °C, then, the temperature stays between 70 °C and 75 °C. After the addition of thiourea, the process lasts about 10 minutes, but the sample must be taken away before the solution becomes completely opaque. At the end of the deposition, the sample is rinsed with deionized water, it is sonicated for 5 minutes and finally dried with a nitrogen stream.

3.3   Surface modification with platinum

Photo-electrodeposition (PED) was performed for depositing Pt using a three-electrode PEC system, this was done to promote the hydrogen evolution reaction. PED activates additional charge-transfer path utilizing electrons photo-excited to the CB. Fine and dispersed particles were electrodeposited under illumination, indicating the nucleation process was prevailing, allowing a better distribution of Pt on the surface of the semiconductor and improving the photocurrent density, charge transfer, and photoconversion of the photocatalyst. The working electrode were CCZTS and CZTS, the anode made of mixed metal oxides (MMO) as counter electrode, and Ag/AgCl in 3 M KCl solution as the reference electrode. These electrodes were submerged in a solution containing 1 mM H_2PtCl_6. The PED took place in potentiostatic condition (at -0.1 V vs. Ag/AgCl for 10-30min) with constant illumination using ABET SunLite solar simulator 11002, provided by a 100 W Xenon arc lamp with 1 sun power and AM 1.5G filter. The deposition was performed with potentiostat/galvanostat AMEL 2559.

3.4   Testing and material characterization

3.4.1 X-Ray diffraction (XRD)

XRD is a technique used to study the crystallographic structure of a material and can provide information on unit cell dimensions, different phases, crystal orientation, grain size, presence of defects and other structural parameters of the analyzed sample. It is based on constructive interference of monochromatic X-rays and a crystalline sample.

Figure 24 shows the basic principle of XRD technique. The interaction of the incident rays with the sample produces constructive interference (and a diffracted ray) only when Bragg's Law ($n\lambda=2d \sin\Theta$) condition is satisfied. In the equation, n is an integer number, λ is the wavelength of the incident radiation, d is the distance between consecutive atomic planes generating diffraction, and ϑ is the angle between the sample's surface and the incoming X-rays. By scanning the sample through a range of 2Θ angles, all possible diffraction directions of the lattice should be attained due to the random orientation of the powdered material. Diffraction peaks are converted into d-

spacings quatities allowing the identification of the mineral because each mineral has a set of unique d-spacings.
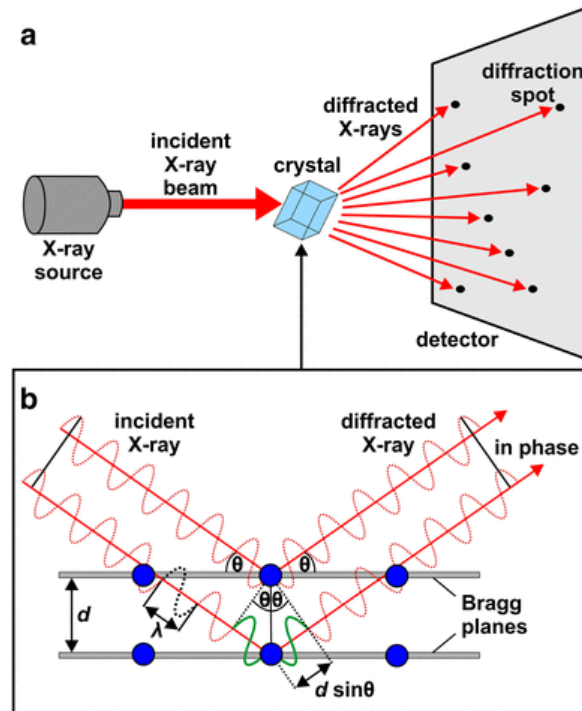
Figure 24. a Basic scheme of an X-ray diffraction experiment. An incident X-ray beam enters the crystal, and the diffracted rays produce a diffraction pattern (diffraction spots), which are recorded on a detector. b Diffraction according to Bragg's Law. Constructive interference is depicted. [50]

The graph with constructive interference pattern is transposed onto an intensity vs angle (2Θ) plot for easier interpretation. For this work, Malvern Panalytical EMPIREAN diffractometer was used. Tests were performed in thin film mode, using a Cu target to generate X-Rays.

3.4.2 Scanning Electron Microscopy (SEM) and Energy Dispersive X-ray Spectroscopy (EDS)

SEM produces images of a sample surface by scanning the surface with a focused beam of electron. In order to generate the beam, a tungsten filament is heated until its electrons are thermionically ejected due to the high energy they possess, and then directed towards the sample under analysis. There are two modes of electron detection

which allows for different types of imaging and analysis. Secondary electrons, emitted close to the surface of the sample, give information about the surface topography. The other kind of electrons are the Backscattered ones, they can be detected to give contrast based on different chemical compositions across an image.

Figure 25 shows the SEM principle. Electrons are generated at the top of the column and then accelerated under vacuum, which helps to prevent any atoms and molecules present in the column from interacting with the electron beam and ensures good quality imaging.

The path of the electrons is controlled by electromagnetic lenses. The condenser defines the resolution by the size of the electron beam, while the objective lens' and scanning coild main roles are the focusing of the beam and raster it onto the sample respectively. The size of the beam is controlled by combining apertures with the lenses. [51]
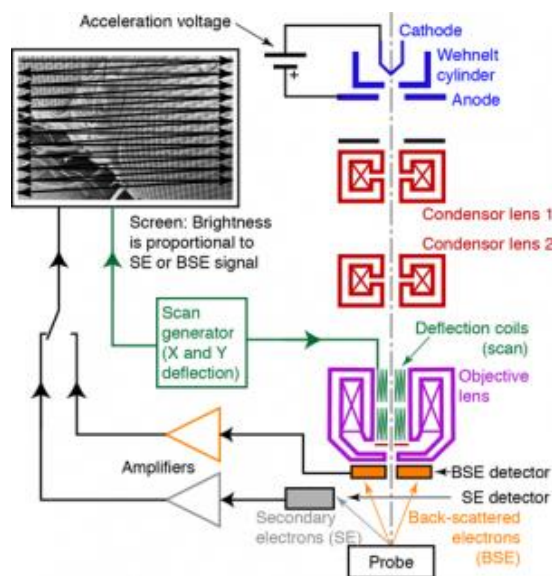
Figure 25. Scanning electron microscopy (SEM) working principle. [52].

Sometimes it is possible to observe the emission of X-rays or Auger (secondary) electrons, based on the energy possessed by the primary ones upon collision with the surface. When exposed to the electron beam, an atom emits characteristic X-rays unique to its atomic number. This allows a sample's elemental composition to be analysed by Energy-dispersive X-ray spectroscopy (EDS). For this work, ZEISS EVO 50 EP, equipped with an OXFORD INCA ENERGY 200 EDS unit was used.

3.4.3 Solar Simulation

The solar simulator used for all the tests is an Abet Technologies' model 11002 SunlineTM solar simulator. This solar simulator utilizes an optimized optical system to deliver an AM1.5 (100 mW/cm2) sun irradiance over an area of 50x50 mm, using a 100 W Xe arc lamp.

3.4.4 Linear Scan Voltammetry (LSV)

Linear scan voltammetry (LSV) is an analysis method in which the current at a working electrode is measured while the potential between the working electrode and a reference electrode is swept linearly in time. This technique consists of a 3 electrode system, working electrode, counter electrode, and reference electrode. The electrodes are placed in an electrochemical cell containing the solution of interest, and are connected to a potentiostat. The potentiostat controls the potential between the working and reference electrodes and measures the current at the working electrode so that a plot can be made that shows the electrochemical response (oxidation or reduction) of the material in question.

Photoelectrochemical testing by linear scan voltammetry was performed with Amel 2559 galvanostat/potentiostat. Samples were tested in a 3 electrodes configuration with CZTS photocathode as WE, Mixed metal oxides (MMO) net as CE and a Ag/AgCl (3M) reference electrode. The electrolyte was an aqueous solution containing 0.5 M phosphate buffer and 0.5 M Na_2SO_4 at pH 7. Samples were illuminated from the front and backside with the solar simulator.

By imposing a decreasing potential, every peak with negative current values can be associated to a reduction phenomenon, while positive current ones indicate oxidation reactions. For this work, LSV was the main technique used to find the photoelectrochemical current and efficiency of the samples produced for potential use in PEC systems for water splitting. In this case, higher values (more negative) of cathodic current corresponds to higher photocurrent density produced and better performance of the material.

4. Results and discussion

4.1   Material characterization

In the following figures, it is possible to see the results obtained for the composition of CZTS and CCZTS calculated from the EDS analysis as a function of these ratios used in the precursor composition:
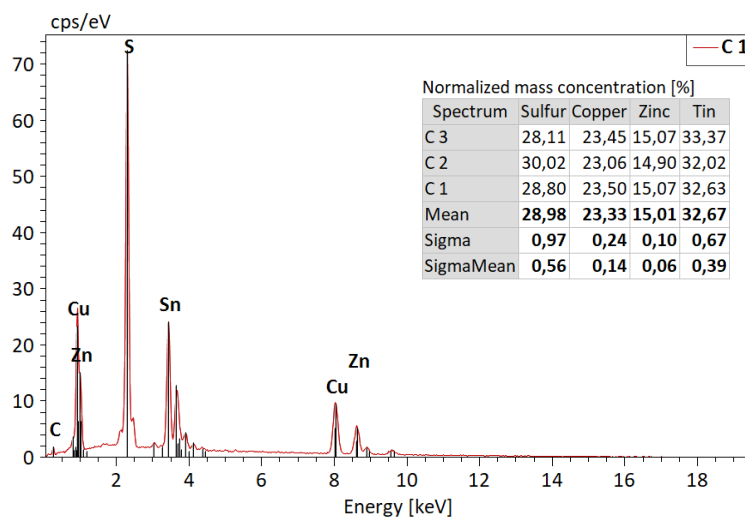
Figure 26. EDS spectrum of CZTS and atomic concentration of the three samples.
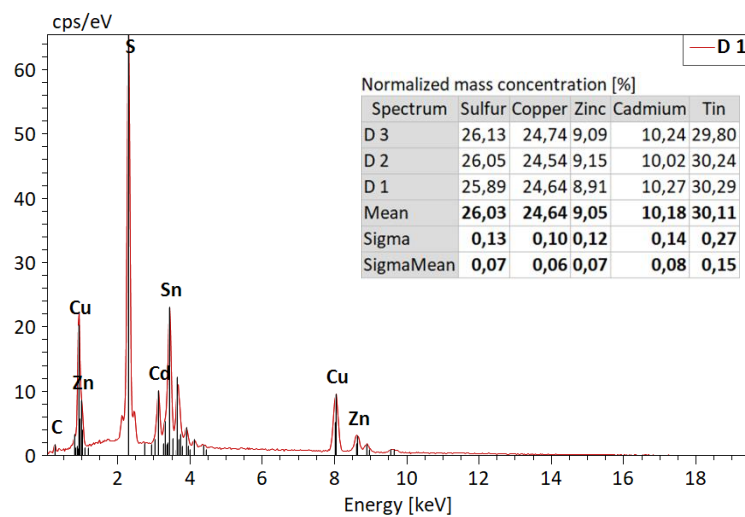
Figure 27. EDS spectrum of CCZTS and atomic concentration of the three samples.

With the EDS, the atomic and normalized mass concentrations for CZTS and CCZTS were obtained with the following results:

Table 2. Atomic ratios for CZTS and CCZTS.

Composition		
Ratio	CZTS	CCZTS
Cu/(Zn+Sn+Cd)	0.727	0.803
(Zn+Cd)/Sn	0.834	0.903
Cd/(Zn+Cd)	0	0.395
S/metal	1.036	0.933

The material should be created with Cu-poor and Zn-rich composition, that is because this improves the efficiency of CZTS solar cells due to formation of shallow acceptor levels of Cu vacancies in CZTS leading to p-doping, while Zn-rich conditions prevent the substitution of Cu on Zn sites, which gives rise to relatively deep acceptor levels. The calculated acceptor (0/-) transition energy level for V_{Cu} is at 0.02 eV above the VBM, whereas for Cu_{Zn} is at 0.10 eV above the VBM. (Figure 28). This can be explained by the fact that the p−d coupling for Cu_{Zn} is enhanced, whereas it is reduced for V_{Cu}, thus the acceptor level of V_{Cu} is shallower [53]. To maximize the absorber performance, growth of Cu_2ZnSnS_4 under Cu-poor and Zn-rich conditions will be optimal, if the precipitation of secondary phases can be avoided. However, in this case, Cu/(Zn+Sn+Cd) and (Zn+Cd)/Sn were lower than in the precursor, possible because an extra Sn signal from SnS_2, SnS, or substrate, this will be confirmed with the XRD tests.
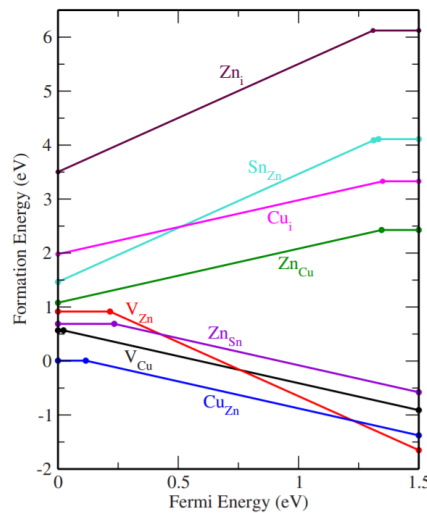
Figure 28. Formation energy of intrinsic defects as a function of the Fermi energy at point which all intrinsic defects have positive formation energies. [53]

Looking at the exact composition values for CCZTS, the Cu/(Zn+Sn+Cd), (Zn+Cd)/Sn, and Cd/(Zn+Cd) are close to the ideal values of 0.8, 1.2 and 0.4 respectively, especially, the ratio Cd/(Zn+Cd) is almost the same, so the doping with Cd was performed correctly. However, these values can be optimized. The Sn content is too high, decreasing its quantity the (Zn+Cd)/Sn and the Cu/(Zn+Sn+Cd) ratios can increase achieving values that are closer to the ideal ones. This difference can be explained due to the sulfurization annealing in the oven, precursors were put inside the graphite box where it is sulfur and metallic Sn but the last has a high vapor pressure and tends to go away from the samples, for this reason it was necessary to put Sn inside the graphite box but the quantity was slightly higher decreasing the (Zn+Cd)/Sn and the Cu/(Zn+Sn+Cd) ratio more than expected due to Sn sulfides formation.

It is true that Cu-poor and Zn-rich material is better but there is a limit because it is also observed a decline in Egap with the increase in Cu/(Zn + Sn) [48], and considering that the CZTS bandgap is 1.5eV, the idea is not to increase it taking into account that the ideal bandgap for a solar cell has a direct band gap of 1.4 eV to absorb the maximum number of photons from the sun's radiation.

Slightly difference in composition and morphology can be attributed also to the lower temperature of pre heating step on the plating of layers in spin coating that was used. The prepared sol solution was spin coated at 3,000 rpm for 30s followed by preheating at 200°C for 2 min on a hot plate in air. Using 280°C as shown by Ying Fan Tay et al. can result in better crystallinity, larger grains, and improved surface morphology with less oxygen content. Nevertheless, the oxygen content is not so high, XRD did not show relevant peaks associated with CdO.

the problem was that microcracks were observed when the samples were heated at this higher temperature.

XRD was performed to identify the structure of the samples and look for possible secondary phases that can affect the performance of the absorber material.
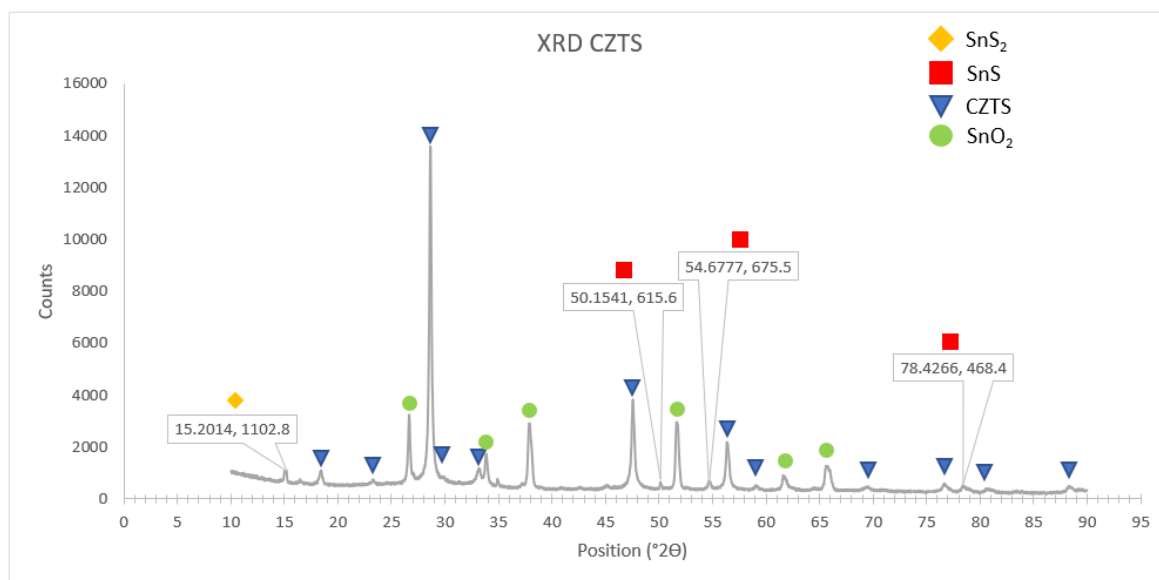
Figure 29. XRD for CZTS.
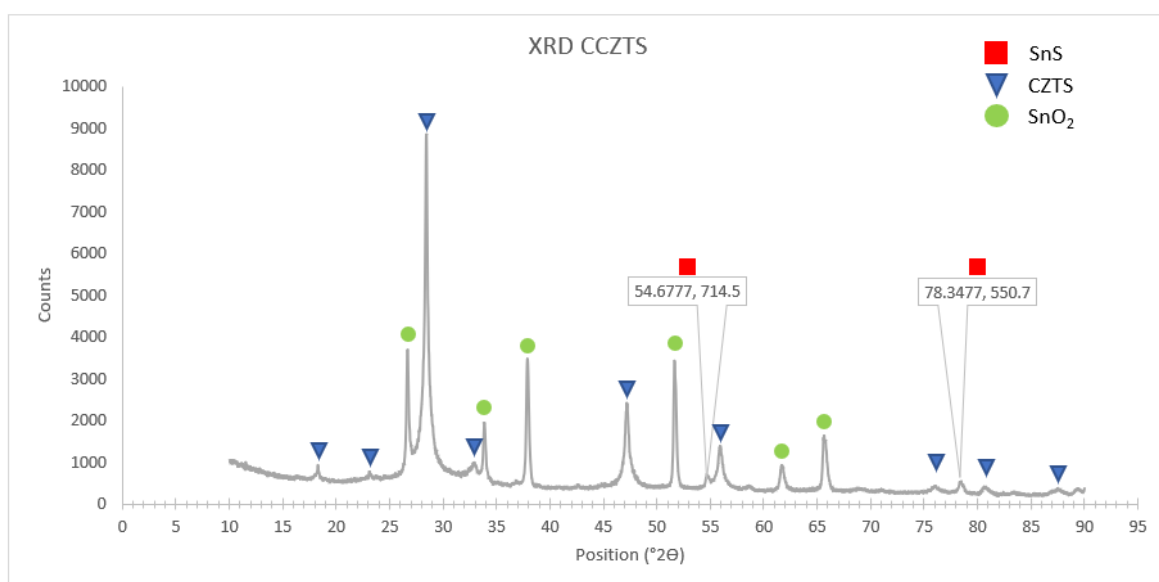
Figure 30. XRD for CCZTS.

The XRDs show that the structure achieved corresponds effectively to that of CZTS kesterite with its main characteristic peaks at 28.5°, 47.3°, and 56.1°. Theoretically, the existence region of single phase kesterite CZTS is rather small, therefore secondary phases such as Sn_xS, Cu_xS, ZnS, or Cu_2SnS_3 appear in CZTS thin films. This situation can be seen in the XRD, there are three peaks at 50.1°, 54.6° and 78.7° that can be attributed to SnS [54] and one peak of SnS_2 at 15.2° [55]. Although relative intensities

54

of all the peaks matching with the kesterite phase are higher than the intensities of the peaks due to secondary impurity phases, it is important to take them into account since for example SnS$_2$ is a kind of compound with high resistivity generating lower carrier concentration of the films. There are also some SnO$_2$ signals coming from the FTO substrate. Furthermore, it is important to consider that ZnS XRD diagram is really close to the CZTS one, peaks superimposition prevents from distinguishing them, so it is possible that some ZnS was present in the sample affecting the performance of the material. The formation of ZnS second phase on the CZTS surface has harmful effects decreasing the conversion efficiency by 2%, it can deteriorate the photovoltaic power conversion efficiency from 10.2% to levels of 8.8%, depending on the material buffer layer and the thickness of ZnS second phase [56]. These secondary phases can be detrimental to the device performance because the ZnS phase can block current flow and introduce dead areas, while SnS phase has lower bandgap than CZTS phase modifying the interface properties.

Here the sulfurization temperature plays a major role, with the increase of the sulfurization temperature, Sn and Zn are diminished seriously resulting in an increase in the carrier concentration, and a decreased in the resistivity [54]. For this reason, it is important to use a sulfurization temperature higher than 500°C.
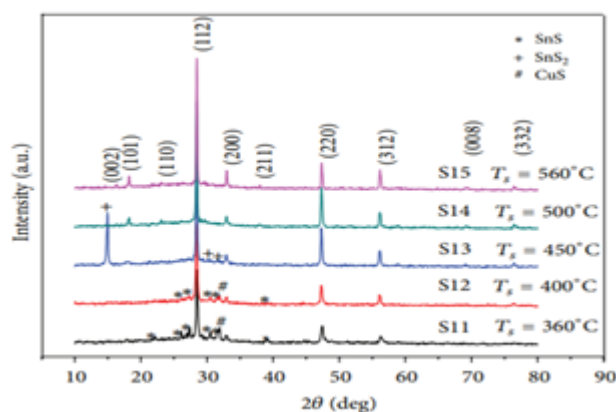
Figure 31. The XRD patterns of the CZTS films obtained at different sulfurization temperatures. [55]

There is also a small shift in the (112) XRD peak from 28.65°C to 28.4°C showing the expansion in crystal lattice as the larger Cd^{+2} ion replaces Zn^{+2}. This can be proved also using the full width at half maximum (FWHM) of the main peak to show the size D of the crystallites determined from XRD data by the Scherrer formula:

$$D = \frac{K\lambda}{\beta \cos\theta}$$

Where K is a dimensionless shape factor, with a value close to unity. The shape factor has a typical value of about 0.9, but varies with the actual shape of the crystallite, β is full width at half maximum (FWHM) in radians, λ is the wavelength of X-ray, and θ is the Bragg angle [57]. Furthermore, the interplanar spacing can be determined using the Bragg's Law:

$$d = \frac{\lambda}{2sin\theta}$$

Studying the main peak for CZTS and CCZTS, crystallite size and interplanar spacing were determined:

Table 3. Data for Crystallite size D calculation.

Sample	CZTS	CCZTS
Angle 2Θ (°)	28.65	28.4
Lamda λ (nm)	0.15406	0.15406
Interplanar spacing d_{hkl} (nm)	0.3113	0.3140
k	0.9	0.9
FWHM (rad)	0.003126	0.002679
Crystallite size D (nm)	45.8	53.4

Table 3 shows an increase in the interplanar spacing but also an increase in the crystallite size of about 17%. From the point of view of the efficiency it is good because increasing the crystallite size can result in a bigger grain size, meaning there are less grain boundaries that normally tend to decrease the electrical conductivity of the material, strongly affect the growth process, and the number of voids in the absorber layer, which are critical to the efficiency enhancement. This will be evaluated using SEM images.

SEM images give information about the possible secondary phases and grain size of the material.
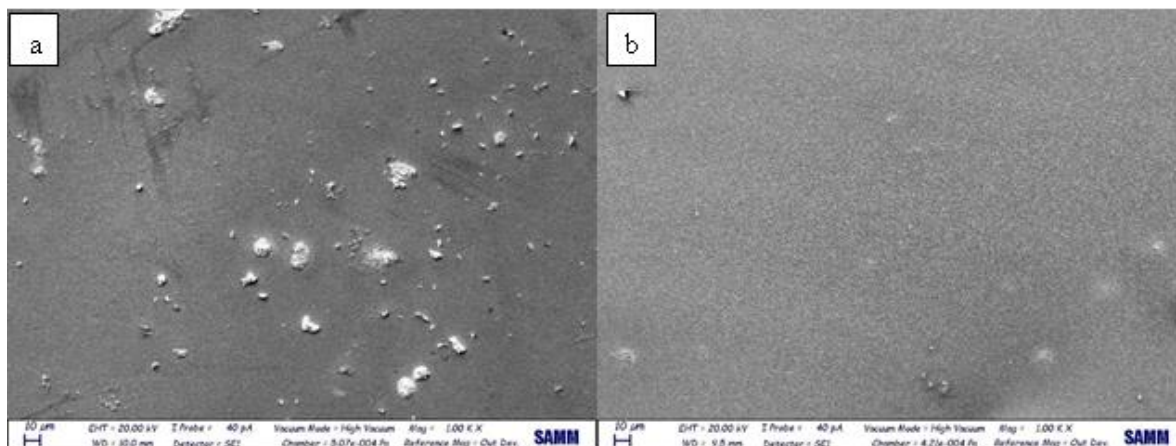
Figure 32. SEM Images of 1kX of (a)CZTS and (b)CCZTS.

In figure 32(a) it is possible to see SnS_x phases on the material, as was expected with the XRD results, on the other side, figure 32(b) shows that CCZTS material is more homogeneous without large zones of secondary phases that can change the properties of the material. CCZTS thin film showed a compact and uniform image, indicating that its crystalline quality was optimized.
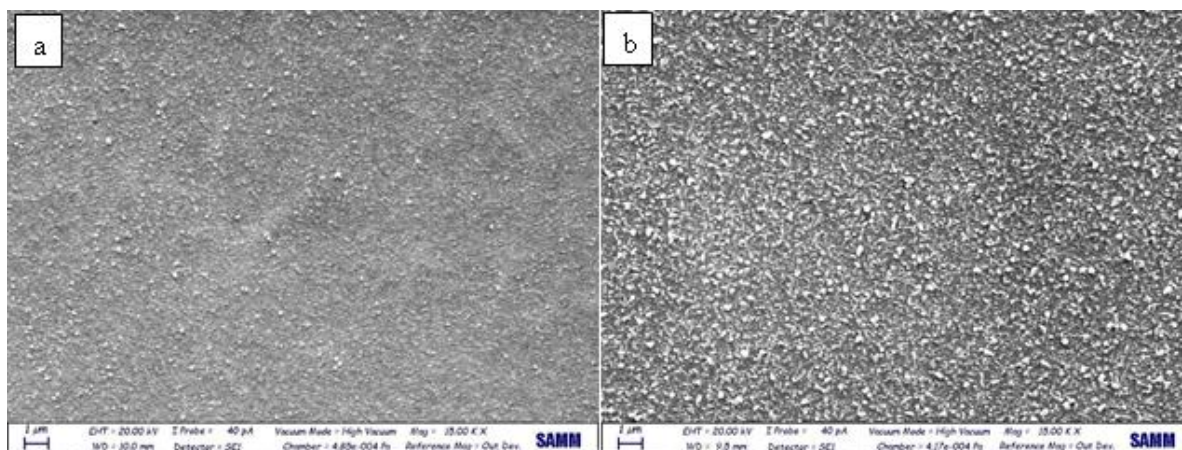
Figure 33. SEM Images of 15kX of (a)CZTS and (b)CCZTS.
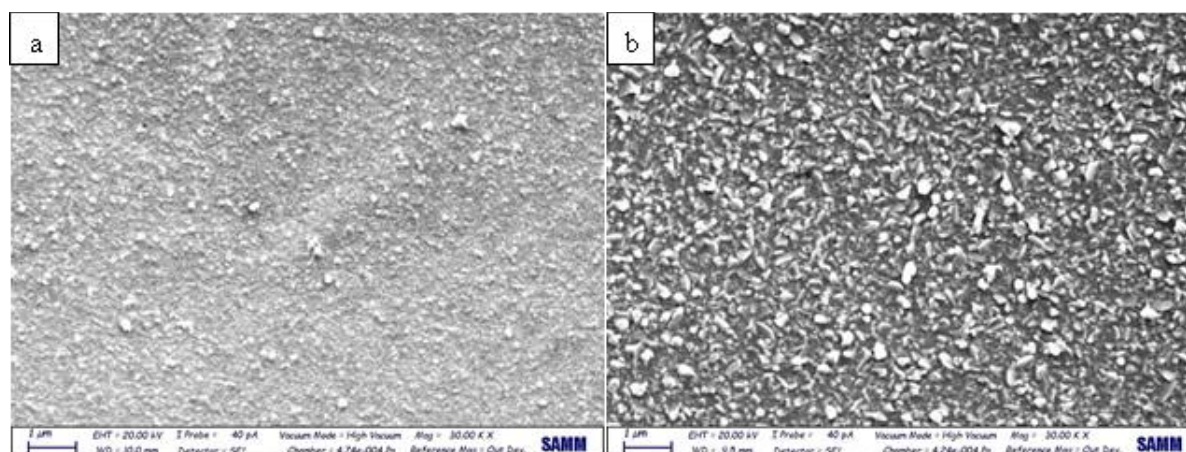
Figure 34. SEM Images of 30kX of (a)CZTS and (b)CCZTS.

On figure 33 and figure 34, the change in the surface relief and particle size can be seen, meaning that, replacing Zn by Cd has a synergistic effect of not just improving the ordering of the crystal atoms but also increasing the grain size from approximately 100nm in CZTS to 200nm in CCZTS.

4.2 Photoelectrochemical testing

To see the performance of the absorber material, linear scan voltammetry was applied. The production rate of hydrogen was not measured and only the photocurrent density was recorded at different values of the electrode potential. However, during the tests, small bubbles were visible, especially when the current density was high, so hydrogen evolution was occurring. Figure 35 show the photocurrent density vs. potential curve for the optimized 13 layers CZTS, and CCZT photocathode coated with CdS/Pt under front illumination of simulated sunlight (AM 1.5G).

The photocurrent measured at -0.6V vs. Ag/AgCl reference electrode was used for the comparison of different samples, corresponding to 0 V vs RHE, thermodynamic potential of hydrogen evolution. Conversion to RHE reference is a convention used to compare samples tested at different pH and with different reference, following the Nernst equation:

$$E_{RHE} = E_{Ag/AgCl} + 0.059pH + E^o_{Ag/AgCl}$$

Where E_{RHE} is the converted potential vs. RHE, $E^o_{Ag/AgCl}$ = 0.1976 at 25 °C, and $E_{Ag/AgCl}$ is the experimentally measured potential against Ag/AgCl reference. [58]

$$0V = E_{Ag/AgCl} + 0.059 * 7 + 0.1976$$

$$-0.610V = E_{Ag/AgCl}$$

The analysis under chopped illumination allows to obtain the plot of the current density in the dark and under illumination during one single test, but several transient peaks, which are a consequence of the initial accumulation of photogenerated charges then partially consumed by recombination, may disturb the reading of the data, because they do not show the performances of the photoelectrode under steady-state conditions [56]. For these reasons here we used a continuous measurement of the photocurrent density since results at dark were closed to zero and because two consecutives measurement using chopped illumination will be probably altered by the polarization of the photoelectrodes during tests. Finally, one measurement from the front and one from the substrate side were taken in order to study the performance of the materials and the PEC device.
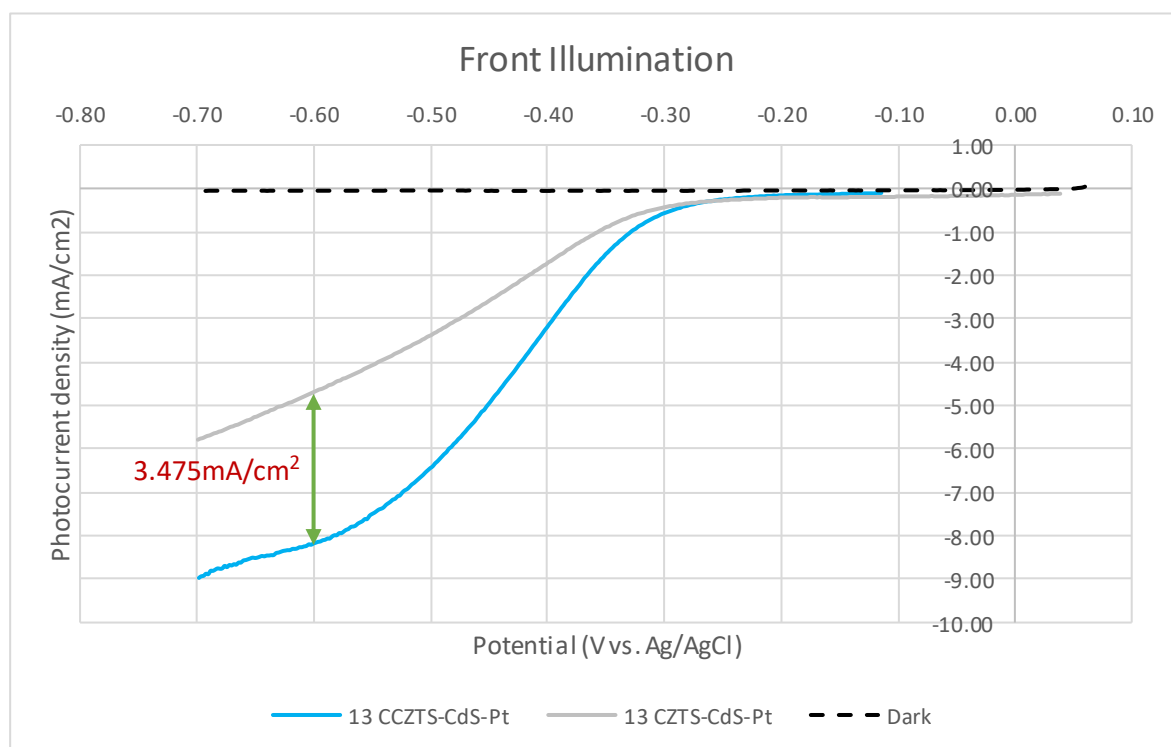
Figure 35. Effect of Cd doping in the photoelectrochemical performance of CZTS/CdS/Pt 13 layers photocathode.

As expected, and following the literature [49], Figure 35 shows a significant enhancement of photocurrent from -4.7045 mA/cm² to -8.1795 mA/cm² at -0.6 V vs Ag/AgCl when Cd substitution was introduced into CZTS kesterite films, also using 10 min Pt photodeposition as a catalyst for hydrogen evolution reaction, the effect of Pt deposition time will be analyzed later. It was also observed that Cd substitution decreases the onset potential of the photocurrent, requiring more cathodic potentials to be applied before appreciable photocurrent of at least 1 mA/cm² can be achieved, this can be due to an unfavorable band alignment of the CCZTS absorber with respect to either CdS buffer layer or the water reduction potential.

Figures 36 and 37 show the photocurrent density vs. potential curve for different layers of CCZT photocathode coated with CdS/Pt under front illumination of simulated sunlight (AM 1.5G).
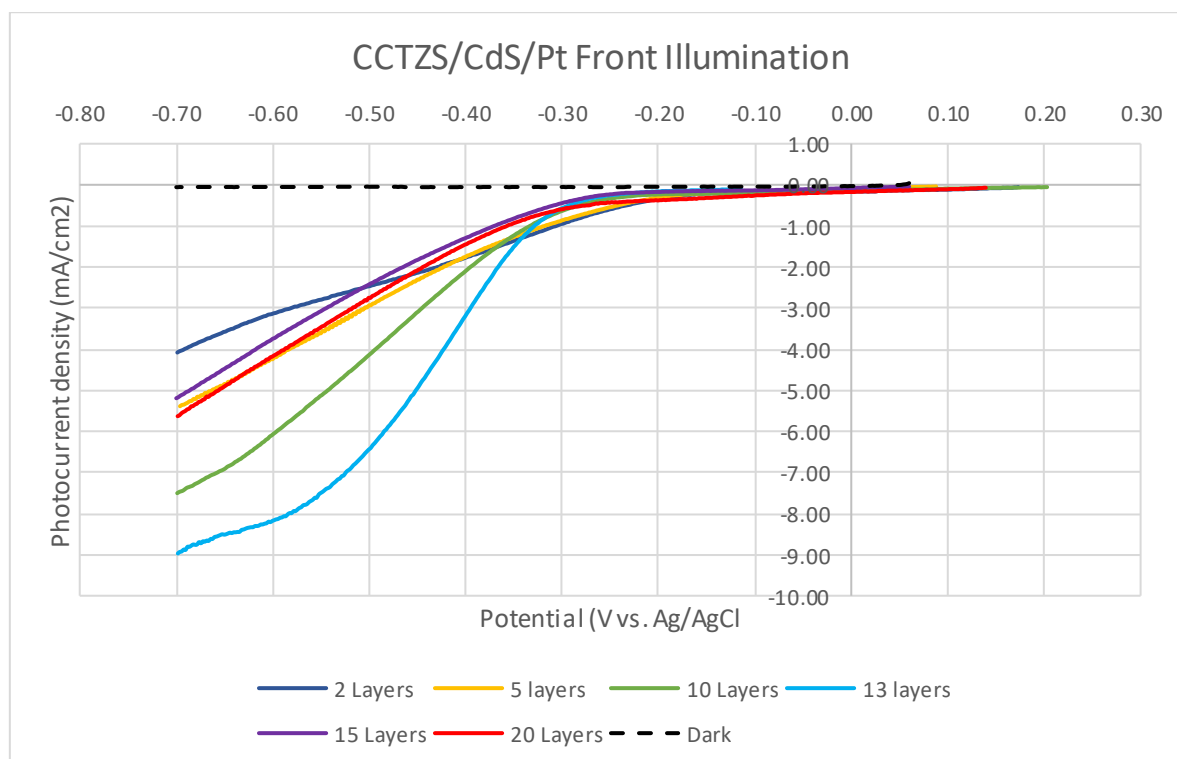
Figure 36. Front illumination photoelectrochemical performance of CCZTS/CdS/Pt photocathode varying the number of layers.
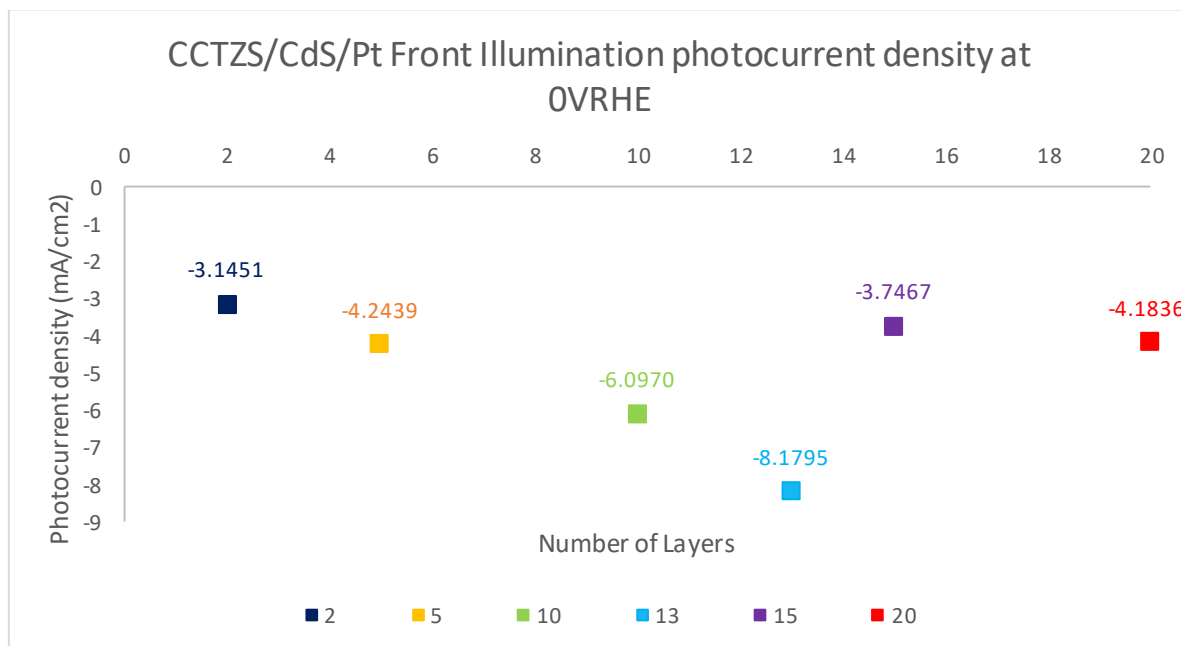
Figure 37. Front illumination photoelectrochemical performance of CCZTS/CdS/Pt photocathode varying the number of layers at 0VRHE.

It can be seen that the photocurrent density increases in absolute value when the electrode potential is more cathodic. At 0V Ag/AgCl its value is about -0.1 mA/cm², while the greatest value at -0.6V Ag/AgCl or 0VRHE is about -8.18 mA/cm² for the optimized CCZTS-CdS-Pt with 13 layers.

In front illumination, deposition of a low number of layers gave low photocurrent density of -3.1451 mA/cm² for 2 layer and -4.2439 mA/cm² for 5 layers. The photocurrent increases with the number of layers up to -8.1795 mA/cm². This happens because below a certain thickness, the photoactive film is not able to absorb enough of the radiation coming from the solar simulator and cannot therefore produce a number of charged species comparable with the ones originated by thicker deposits. However, this raise in the performance of the absorber material does not keep increasing continuously without a limit, there is a maximum number of layers depending on the composition in which the carriers must cover a longer distance and increasing the layers will increase the probability of recombination events.

Another aim of this work is to analyze the performance of the absorber material when it is illuminated from the back, through the transparent substrate. Figure 38 shows the photocurrent density in back illumination vs the potential vs Ag/AgCl. At -0.6V vs

Ag/AgCl, the values for back illumination are lower than for front illumination. The maximum value for front illumination is 179% higher than the one for back illumination. Figure 39 shows a comparison between all the curves just to have the idea of the differences depending on the side where the light is coming.
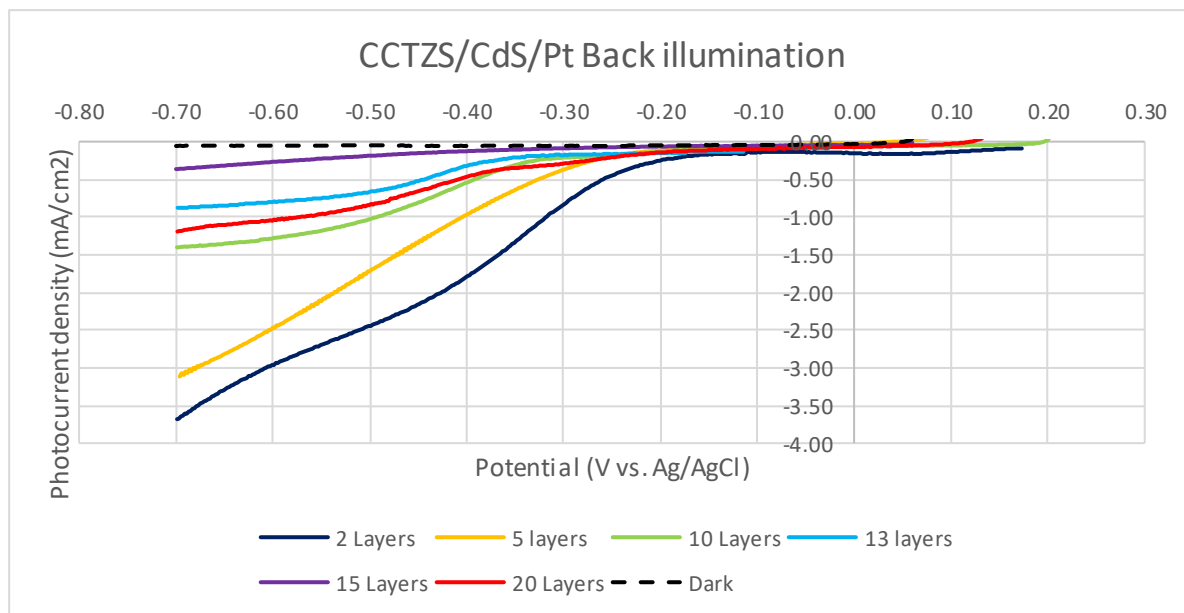
Figure 38. Back illumination photoelectrochemical performance of CCZTS/CdS/Pt photocathode varying the number of layers.
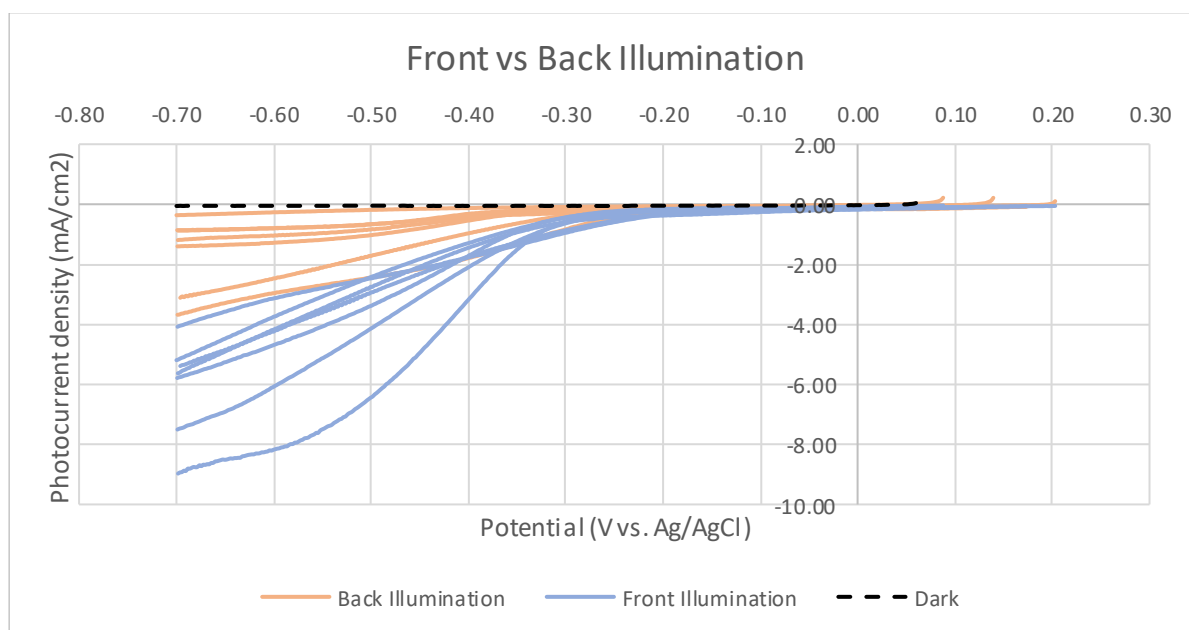
Figure 39. Photoelectrochemical performance of CZTS photocathode in front and back illumination.

Now, it is important to observe the trend for back illumination photocurrent density with respect to the number of layers. Figure 40 shows a clear trend of decreasing the photocurrent density with the increase in the number of layers of the material. However, as it was seen in Figure 39, the value for the maximum photocurrent density is much lower in this case.
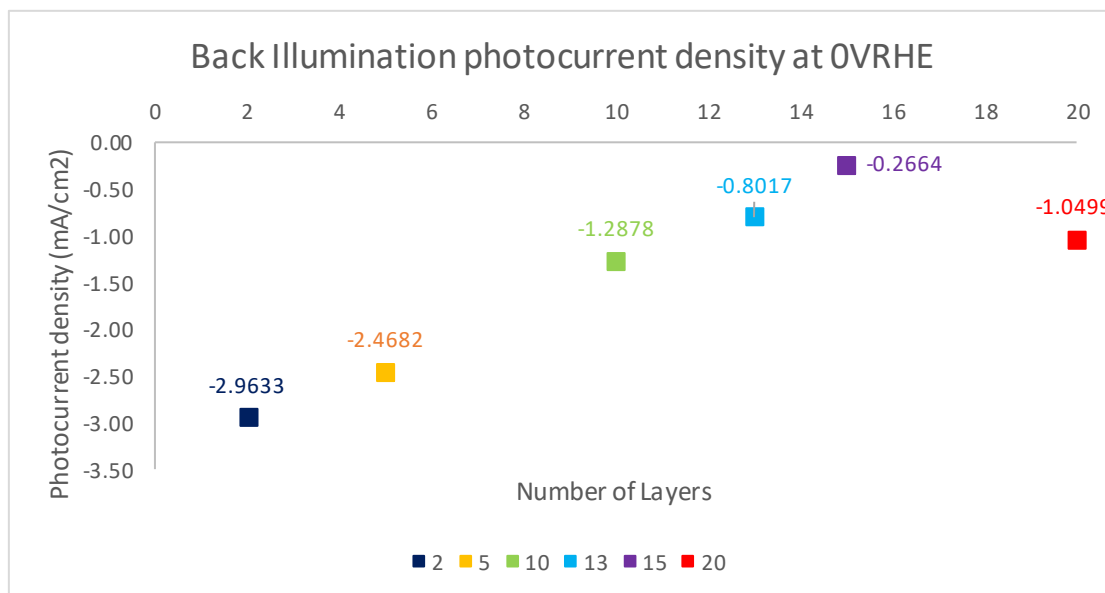
Figure 40. Back illumination photoelectrochemical performance of CCZTS/CdS/Pt photocathode varying the number of layers at 0VRHE.

This difference with respect to the front illumination is because in back illumination photo-charges are formed closer to the substrates, so electrons have a longer path to the surface. for this reason, the trend is inversed. Furthermore, in back illumination the path is shorter for a minor thickness. However, the overall photocurrent is lower because a thinner material absorbs less light. In fact, 2-layer samples are brownish and transparent, thicker ones are darker and almost opaque, they absorb almost all the impinging light. Figure 41 illustrates the comparison of the maximum photocurrent density for each number of layers.
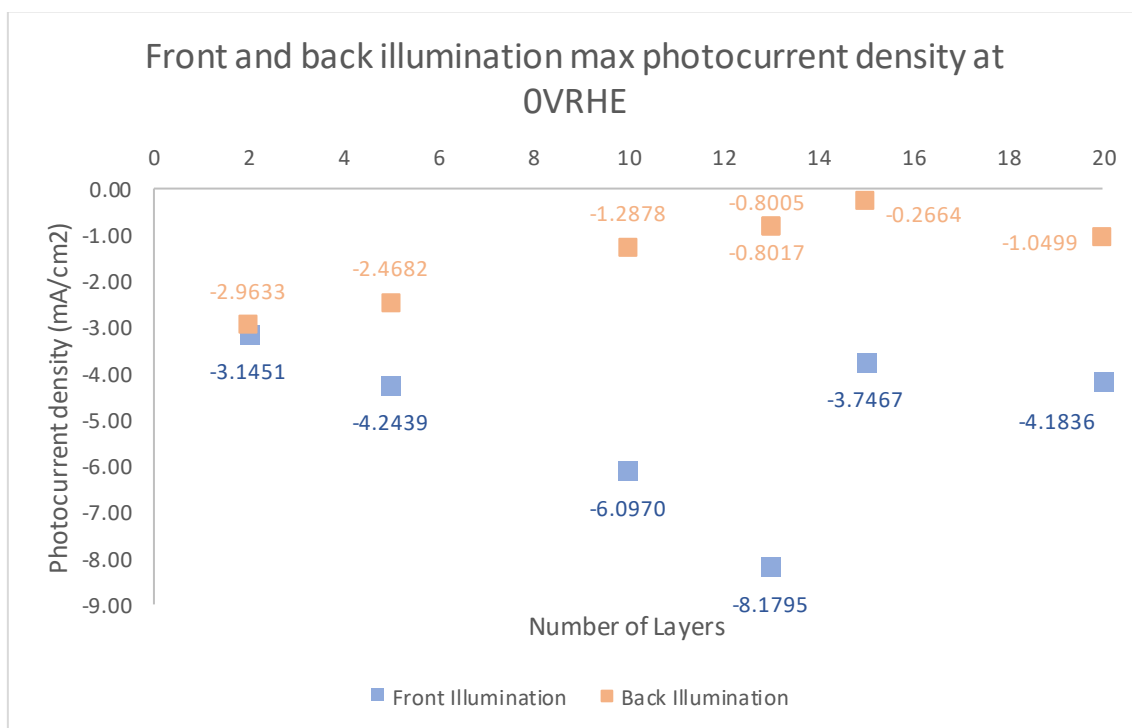
Figure 41. Front and Back illumination photoelectrochemical performances for different layers.

In order to promote the hydrogen evolution reaction, platinum nanoparticles were deposited onto the surface of the photocathodes by photoelectrochemical deposition (PED). The effect of Pt deposition time on the CCZTS performance is going to be studied. Based on the previous results, 2 layers was used especially for back illumination and 13 layers was used to study the Pt effect in front illumination. However, the samples were always tested from both sides.

Figures 42 and 43 show the performance of CCZTS/CdS/Pt for the 2 layers sample in front and back illumination. As it was expected, the photocurrent density achieved was higher in the case of back illumination with -5.2 mA/cm² against -3.63 mA/cm² in the case of front illumination, so it means 43% higher thanks to the lower distance the electrons must travel to reach the substrate. Furthermore, the best performance was achieved with Pt deposition time of 20min, neither the lower, nor the higher.
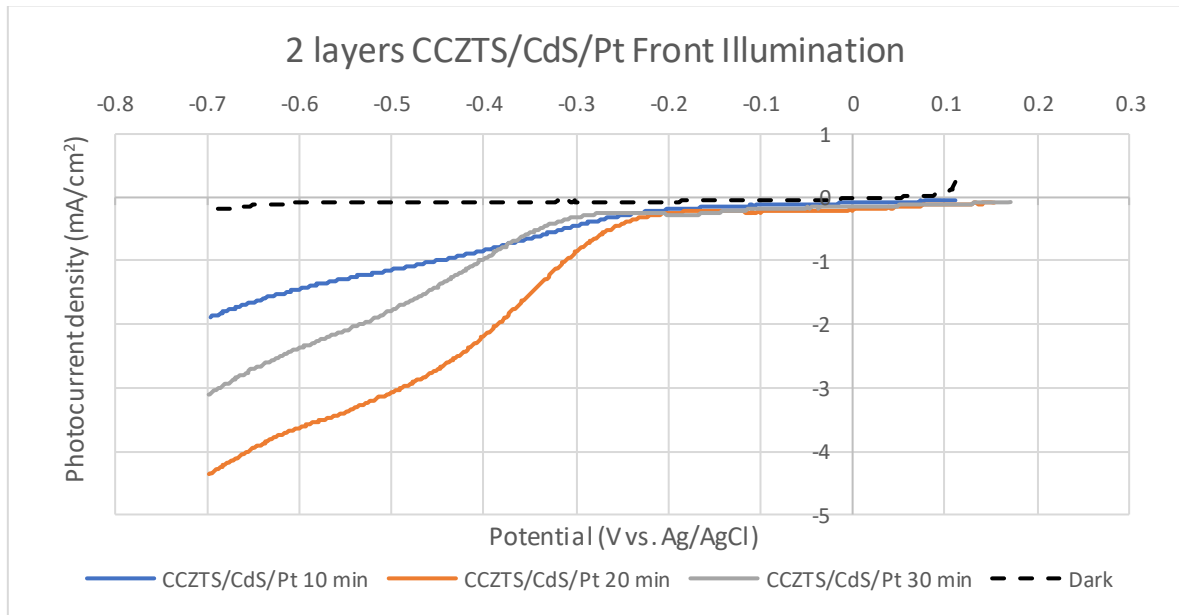
Figure 42. Front illumination photoelectrochemical performance for 2 layers CCZTS/CdS/Pt. at different Pt PED times.
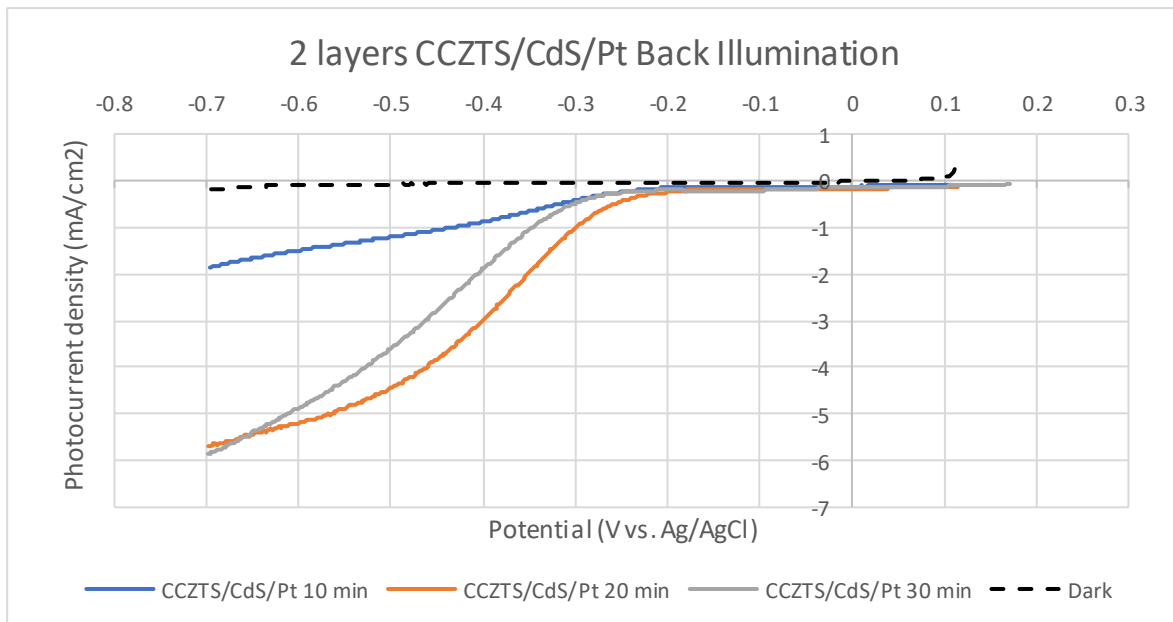
Figure 43. Back illumination photoelectrochemical performance for 2 layers CCZTS/CdS/Pt at different Pt PED times.

The same situation respecting the Pt deposition time was obtained for the CCZTS/Cd/Pt 13 layers sample. In the case of 13 layers, the front illumination will be higher due to thicker absorption volume, achieving almost 4 times the photocurrent

density obtained with back illumination (-3.37 mA/cm² vs. -0.86 mA/cm²). It is important to observe the trend of the material performance with the increase in Pt. Apart from the fact that Pt is the preferred catalyst for hydrogen generation and increasing its quantity (up to a limit) will benefit the When Pt was deposited on the CCZTS film, sparsely grown Pt dots could be created on the CCZTS film. Rough surface could be built and possibly being in direct contact with the electrolyte enhancing the interfacial photocatalytic activity. In that case, a continuous energetic state can be provided by Pt dots, which facilitated the efficient transport of large number of electrons during the redox reaction. This improvement will increase at the beginning while Pt is being deposited, but there is a limit and keep incrementing the amount of Pt is counterproductive. The clustering effect by the excessive Pt over the surface prevents the absorption of sufficient light by the CCZTS layer, which hindered the generation of electron-hole pairs due to a higher reflection phenomenon. Furthermore, those negative effects are more visible in the front illumination case because the clustering is directly affecting the entry of the light. For these reasons, platinum controlled deposition is recommended, because it can notably improve the performance of the PEC device.
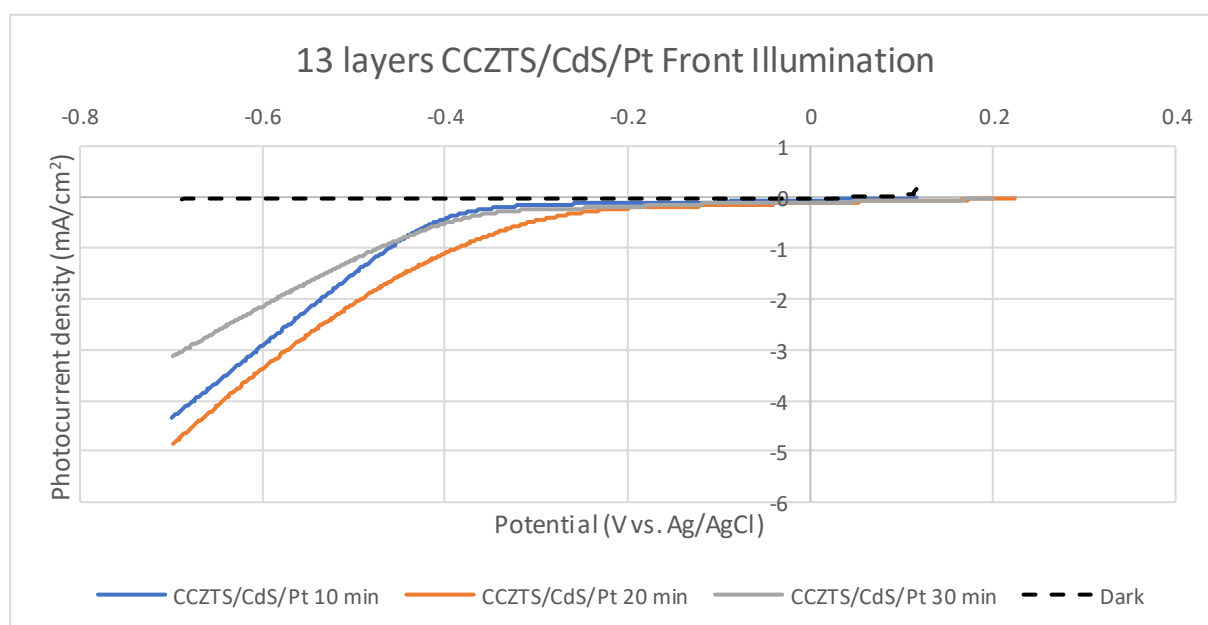
Figure 44. Front illumination photoelectrochemical performance for 13 layers CCZTS/CdS/Pt. at different Pt PED times.
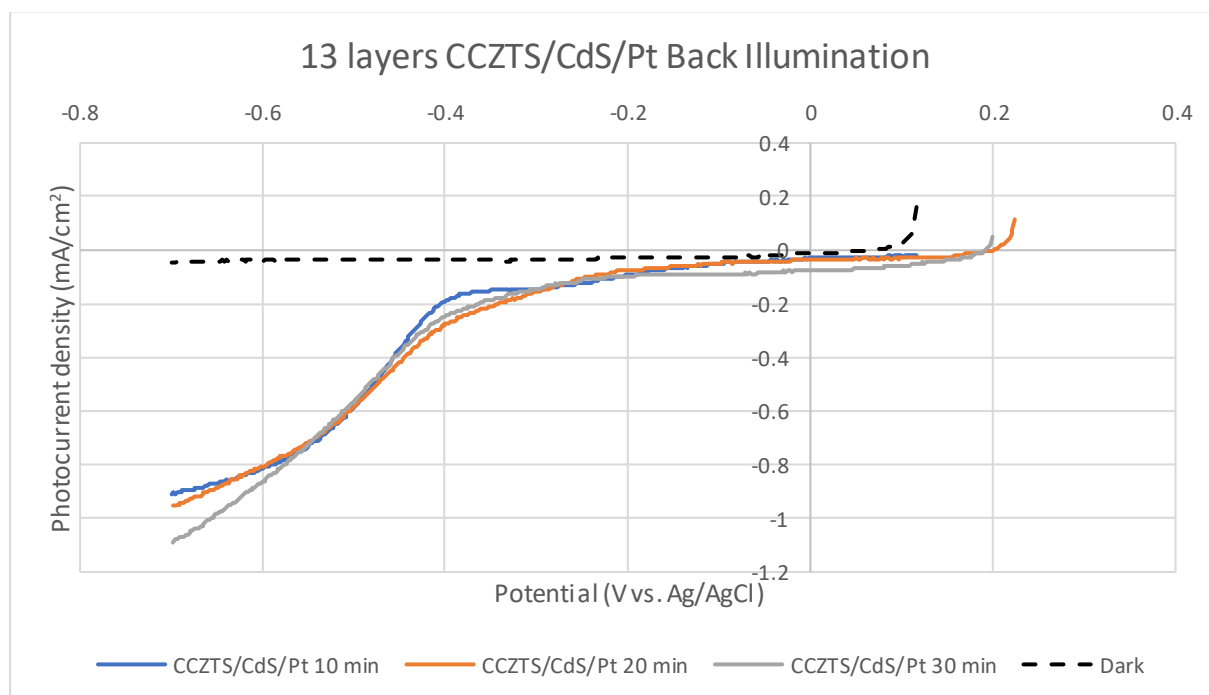
Figure 45. Back illumination photoelectrochemical performance for 13 layers CCZTS/CdS/Pt at different Pt PED times.

Finally, these measurements and the photocurrent density were obtained applying an external bias between the WE and the CE in a two-electrode configuration in order to have the water splitting reaction in the PEC cell. Thus, ABPE (see section 2.6.3) is useful to find the conversion efficiency. ABPE is the IUPAC-suggested definition of the solar conversion efficiency of a cell that has a dark electrode and a semiconductor-based photoelectrode. It measures the net chemical output power of a system in units of incident solar power [59], and it is calculated as the ratio between the electrical output of the electrode (subtracting the external contribution of the applied bias) over the solar energy power input. Due to the interest in build a photocathode that works for back illumination, the ABPE was measured for the 2 layers CCZTS/CdS/Pt in a two-electrode system. Figure 46 shows the ABPE vs. the bias applied. The maximum ABPE was 1.68% at 0.74V applied bias for back illumination, a value that although it is not the 7.2 maximum achieved for CZTS based photocathode by Huang, D et al[60], but for a large scale cost effective PEC device is a promising value that could help in the development of green hydrogen for renewable energy sources.
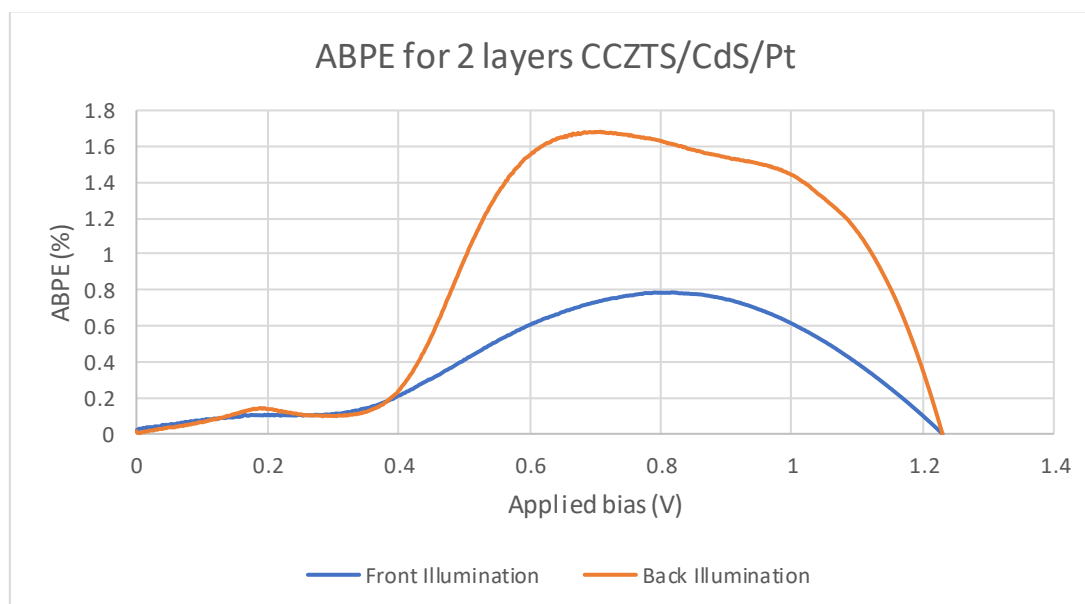
Figure 46. ABPE calculation for 2 layers CCZTS/CdS/Pt (20 min).

5. Conclusions

In the present work, the effects of cadmium doping on copper zinc tin sulfide Cu_2ZnSnS_4 (CZTS) were investigated for water splitting application in a photoelectrochemical cell. CZTS has emerged as a potential absorber towards inorganic photovoltaic device application for its outstanding properties like nontoxicity, optimal Egap matched with solar spectrum (1.5eV), earth abundancy nature, and high absorption coefficient ($10^4 cm^{-1}$). Cd substitution on Zn sites was done as an improvement in CZTS thinking on an alternative for the CIGS/CdS/Pt photocathode, which have the rare element indium, but also, is fabricated using vacuum co-evaporation, a high vacuum challenging technique for large scale production.

The precursor was prepared adjusting Cd and Zn relative quantities so that Cd/(Zn+Cd) = 0.4. In this way, the composition ratios Cu/(Zn+ Cd + Sn) and (Zn + Cd)/Sn were 0.86 and 1.25 respectively in the precursor solutions, and 0.80 to 0.90 in the Cd doped CZTS after sulfurization treatment. The prepared sol solution was spin coated on FTO glass substrates followed by preheating on a hot plate in air. The spin coating was repeated from 2 to 20

times to obtain the desired thickness. CdS was used as a buffer layer and it was deposited onto the absorber material by CBD, and finally, Pt PED was performed at different times to see the consequences of the catalyst deposition.

XRD reveals the effectively CZTS structure of the samples but also some SnS_2 and SnS peaks appeared. A shift in the (112) peak from 28.65°C to 28.4°C showed an expansion in the crystal lattice due to the larger size of Cd^{+2} compared with Zn^{+2}, resulting in 17% crystallite size expansion and also a grain size change from 100nm to 200nm. However, the result could be better (400nm to 700nm) if the preheated were performed at 280°C [49], but the problem was the cracking of the samples at that high temperature. The tin sulfide second phases were confirmed with SEM-EDS analysis where some SnS_x bright spots showed up, but the improvement in the uniformity and homogeneity of the material were also confirmed.

Photoelectrochemical performance was studied with LSV. In the case of front illumination, the photocurrent density obtained increase with the number of layers, Cd doping and Pt deposition allowed to obtain 8.18mA/cm^2 for the CCZTS in front illumination with 13 layers, increasing 73.8%. On the other hand, 2 layers of the photoabsorber was the best scenario for back illumination achieving -2.96mA/cm^2. Higher thickness experiences high recombination of the photo-generated carriers which recombines before reaching the buffer layer/CZTS layer interface. Increasing the thickness, the photocurrent density increases too, because the thicker CZTS layer will absorb more photons and generates more electron–hole pairs. But after a certain thickness, the performance again starts to deteriorate as the CZTS layer crosses its minority carrier diffusion length. For back illumination, lower number of layers is better because of the fast electron extraction to the back contact with lower transport distances.

Pt PED optimum time was 20min with an increase in photocurrent density of 16% for 13 layers front illumination, and 240% for 2 layers in back respect the 10min values. The increase in deposition time of the catalyst could create a rough surface possibly being in direct contact with the electrolyte enhancing the interfacial photocatalytic activity. Nonetheless, keep increasing the deposition time lowers the photocurrent density because of clustering effects that blocked and reflected the light.

A promising ABPE value of 1.68% at 0.74V applied bias was found in back illumination for 2 layers material, showing that there is space for green H_2 generation with PEC device,

but improvement in fabrication reaching higher temperatures without cracking that allows to increase the grain size and decrease recombination sites are needed in order to reach higher efficiencies. Although the efficiencies are not still the best ones, the potential for cheaper renewable hydrogen through device integration, the use of stable and abundant materials, and the use of waste heat to accelerate the electrochemical reactions, provide a strong motivation to continue efforts in developing CCZTS solar water splitting devices.

6. Bibliography

1. International Energy Agency (IEA), Global Energy Review 2021 (Paris: 2021), https://www.iea.org/reports/global-energy-review-2021.
2. REN 21. Renewables 2021 Global status report. (2021). [Online]. Available at: https://www.ren21.net/wp-content/uploads/2019/05/GSR2021_Full_Report.pdf
3. UNEP, "Why does energy matter?" https://www.unenvironment. org/explore-topics/energy/why-does-energy-matter, viewed 2 February 2020.
4. Energy Sufficiency and European Council for an Energy Efficient Economy, Energy Sufficiency and Rebound Effects (Stockholm: 2018), https://www.energysufficiency.org/static/media/uploads/site-8/library/papers/sufficiency-rebound-final_formatted_181118.pdf
5. Chemical Economics Handbook, IHS Markit, 2018.
6. GEI (Global Energy Infrastructure), 2021. Hydrogen – data telling a story. [Online] Available at: https://globalenergyinfrastructure.com/articles/2021/03-march/hydrogen-data-telling-a-story/
7. N.-T. Suen, S.-F. Hung, Q. Quan, N. Zhang, Y.-J. Xu, H.M. Chen, Chem. Soc. Rev. 46(2), 337–365 (2017)
8. Magagnin, L. Hydrogen production [Slides]. (2020). Politecnico di Milano.
9. Kittel, C. (2004). Introduction to solid state physics (8th ed.). John Wiley & Sons.
10. Aldaraghmeh, Tariq. (2013). Study of some electrical properties of undoped lead iodide thin films deposited by flash-evaporation method at substrate temperatures between 150°C and 200°C. 10.13140/RG.2.2.32039.65440.
11. Semiconductors and Energy Level Diagrams. (2021, March 21). Retrieved July 29, 2021, from https://eng.libretexts.org/@go/page/18973
12. Vulpecula. (2009). Schematic plot of Fermi-Dirac distribution. [Online] Available at: https://commons.wikimedia.org/wiki/File:Fermi_dirac_distr.svg
13. Rioult, Maxime. (2015). Hematite-based epitaxial thin films as photoanodes for solar water splitting. 10.13140/RG.2.1.3709.2240.
14. Rajeshwar, Krishnan. (2007). Encyclopedia of Electrochemistry. 10.1002/9783527610426.bard060001.
15. Schmickler W., Santos E. (2010) The semiconductor-electrolyte interface. In: Interfacial Electrochemistry. Springer, Berlin, Heidelberg. https://doi.org/10.1007/978-3-642-04937-8_11
16. R. Memming, "Semiconductor Electrochemistry", 2nd edition, Wiley-VCH, 2015, ISBN 978-3-527-68871-5.

17. C. Jiang, S.J.A. Moniz, A. Wang, T. Zhang, J. Tang, Photoelectrochemical devices for solar water splitting—materials and challenges, Chem. Soc. Rev. 46 (2017) 4645–4660.

18. P. Lianos, Review of recent trends in photoelectrocatalytic conversion of solar energy to electricity and hydrogen, Appl. Catal. B Environ. (2017), https://doi.org/10.1016/j.apcatb.

19. S.Choudhary, S. Upadhyay, P. Kumar, N. Singh, V.R. Satsangi, R. Shrivastav, S. Dass, Nanostructured bilayered thin films in photoelectrochemical water splitting—a review, Int. J. Hydrogen Energy 37 (2012) 18713–18730, https://doi.org/10.1016/j.ijhydene.2012.10.028.

20. L.J. Minggu, W.R. Wan Daud, M.B. Kassim, An overview of photocells and photoreactors for photoelectrochemical water splitting, Int. J. Hydrogen Energy 35 (2010) 5233–5244, https://doi.org/10.1016/j.ijhydene.2010.02.133.

21. Jiang, Chaoran & Moniz, Savio & Wang, Aiqin & Zhang, Tao & Tang, Junwang. (2017). Photoelectrochemical devices for solar water splitting - materials and challenges. Chemical Society reviews. 46. 10.1039/c6cs00306k.

22. Kim, Seunghyeon & Lee, Jae Sung. (2014). BiVO4-Based Heterostructured Photocatalysts for Solar Water Splitting: A Review. Energy and Environment Focus. 3. 10.1166/eef.2014.1121.

23. Kan, Zhang & Ma, Ming & Li, Ping & Wang, Dong Hwan & Park, Jong Hyeok. (2016). Water Splitting Progress in Tandem Devices: Moving Photolysis beyond Electrolysis. Advanced Energy Materials. 6. 1600602. 10.1002/aenm.201600602.

24. Cox, Casandra & Lee, Jungwoo & Nocera, Daniel & Buonassisi, Tonio. (2014). Ten-percent solar-to-fuel conversion with nonprecious materials. Proceedings of the National Academy of Sciences of the United States of America. 111. 10.1073/pnas.1414290111.

25. Parnis, J Mark & Oldham, Keith. (2013). Beyond the Beer–Lambert law: The dependence of absorbance on time in photochemistry. Journal of Photochemistry and Photobiology A: Chemistry. 267. 6-10. 10.1016/j.jphotochem.2013.06.006.

26. Aruchamy, A., Aravamudan, G. and Subba Rao, G. (1982) Semiconductor based photoelectrochemical cells for solar energy conversion – An overview. Bull Mater. Sci., 4, 483-526.

27. Li, Suning & Fu, Jiajun. (2013). Improvement in corrosion protection properties of TiO2 coatings by chromium doping. Corrosion Science. 68. 101–110. 10.1016/j.corsci.2012.10.040.

28. Paracchino, N. Mathews, T. Hisatomi, M. Stefik, S. D. Tilley and M. Gra̎tzel, Energy Environ. Sci., 2012, 5, 8673.

29. Li J, Jin X, Li R, Zhao Y, Wang X, Liu X, Jiao H, Copper oxide nanowires for efficient photoelectrochemical water splitting, Applied Catalysis B: Environmental (2018), https://doi.org/10.1016/j.apcatb.2018.08.070.

30. Kumagai, Hiromu & Minegishi, Tsutomu & Sato, Naotoshi & Yamada, Taro & Kubota, Jun & Domen, Kazunari. (2015). Efficient Solar Hydrogen Production from Neutral Electrolytes Using Surface-Modified Cu(In,Ga)Se2 Photocathodes. J. Mater. Chem. A. 3. 10.1039/C5TA01058F.

31. Lim, H., Young, J.L., Geisz, J.F. et al. High performance III-V photoelectrodes for solar water splitting via synergistically tailored structure and stoichiometry. Nat Commun 10, 3388 (2019). https://doi.org/10.1038/s41467-019-11351-1.

32. M. M. May, H.-J. Lewerenz, D. Lackner, F. Dimroth, and T. Hannappel, Nat. Commun. 6, 8286 (2015). https://doi.org/10.1038/ncomms9286.

33. Mi, Zetian & Shen, Mingrong. (2019). Silicon based photoelectrodes for photoelectrochemical water splitting. Optics Express. 27. A51. 10.1364/OE.27.000A51

34. X. Chen, L. Liu, P. Y. Yu and S. S. Mao, Science, 2011, 331, 746–750.

35. Yang, Yi & Pu, Ying-Chih & Li, Yat & Zhang, Jin. (2016). Oxygen Deficient TiO2 Photoanode for Photoelectrochemical Water Oxidation. Solid State Phenomena. 253. 11-40. 10.4028/www.scientific.net/SSP.253.11.

36. Atabaev, Timur & Hossain, Md & Lee, Dongyun & Kim, Hyung & Hwang, Yoon-Hwae. (2016). Pt-coated TiO2 nanorods for photoelectrochemical water splitting applications. Results in Physics. 6. 10.1016/j.rinp.2016.07.002.

37. Li, F, Jian, J, Xu, Y, Wang, S, Wang, H, Wang, H. Recent advances on interfacial engineering of hematite photoanodes for viable photo-electrochemical water splitting. Engineering Reports. 2021; 3:e12387. https://doi.org/10.1002/eng2.12387.

38. Zhang H, Park JH, Byun WJ, Song MH, Lee JS (2019) Activating the surface and bulk of hematite photoanodes to improve solar water splitting. Chem Sci. 2019;10(44):10436-10444. https://doi.org/10.1039/c9sc04110a.

39. Yang J, Wang D, Han H, Li C. (2013). Roles of cocatalysts in photocatalysis and photoelectrocatalysis. 46(8):1900-1909. https://doi.org/10.1021/ar300227e

40. Mayer, M. T. (2017). Photovoltage at semiconductor–electrolyte junctions. Curr. Opin. Electrochem. 2, 104-110.

41. Kim, Seunghyeon & Lee, Joon. (2019). Elaborately Modified BiVO4 Photoanodes for Solar Water Splitting. Advanced Materials. 31. 10.1002/adma.201806938.

42. Jiang, Jiangang & Wang, He & An, Hongchang & Du, Guangyuan. (2020). Controlled Growth of CdS Nanostep Structured Arrays to Improve

Photoelectrochemical Performance. Frontiers in Chemistry. 8. 10.3389/fchem.2020.577582.

43. Mali, M.G., Yoon, H., Joshi, B.N., Park, H., AlDeyab, S.S., Lim, D.C., Ahn, S., Nervi, C., and Yoon, S.S. (2015). Enhanced photoelectrochemical solar water splitting using a platinum-decorated CIGS/CdS/ZnO photocathode. ACS Appl. Mater. Interfaces 7, 21619–21625.

44. Daisuke, Y., Tsutomu, M., Kazuo, J., Takashi, H., Guijun, M., Masao, K., Jun, K., Hironori, K., and Kazunari, D. (2010). H2 evolution from water on modified Cu2ZnSnS4 photoelectrode under solar light. Appl. Phys. Express 3, 101202.

45. Yang, W., Oh, Y., Kim, J., Jeong, M.J., Park, J.H., and Moon, J. (2016). Molecular chemistrycontrolled hybrid ink-derived efficient Cu2ZnSnS4 photocathodes for photoelectrochemical water splitting. ACS Energy Lett. 1, 1127–1136

46. Kumar, M., Dubey, A., Adhikari, N., Venkatesan, S., and Qiao, Q. (2015). Strategic review of secondary phases, defects and defect-complexes in kesterite CZTS-Se solar cells. Energy Environ. Sci. 8, 3134–3159.

47. Feng, Xiaoyang & Hou, Lulu & Huang, Zhenxiong & Li, Rui & Shi, Jinwen & Chen, Yubin. (2019). A self-doping strategy to improve photoelectrochemical performance of Cu2ZnSnS4 nanocrystal films for water splitting. Chemical Communications. 55. 10.1039/C9CC05232A.

48. Babu, G. & Kumar, Y.B & Bhaskar, P. & Vanjari, Sundara. (2010). Effect of Cu/(Zn+Sn) ratio on the properties of co-evaporated Cu2ZnSnSe4 thin films. Solar Energy Materials and Solar Cells - SOLAR ENERG MATER SOLAR CELLS. 94. 221-226. 10.1016/j.solmat.2009.09.005.

49. Tay, Ying & Kaneko, Hiroyuki & Chiam, Sing & Lie, Stener & Zheng, Qiusha & Wu, Bo & Hadke, Shreyash & Su, Zhenghua & Saurabh, Prince & Bishop, Douglas & Sum, Tze Chien & Minegishi, Tsutomu & Barber, James & Domen, Kazunari & Wong, Lydia. (2018). Solution-Processed Cd-Substituted CZTS Photocathode for Efficient Solar Hydrogen Evolution from Neutral Water. Joule. 2. 10.1016/j.joule.2018.01.012.

50. Bijelic, A., Rompel, A. (2018). Polyoxometalates: more than a phasing tool in protein crystallography. ChemTexts 4, 10. https://doi.org/10.1007/s40828-018-0064-1.

51. Tandon, Gyaneshwar & Pochiraju, Kishore. (2017). Environmental Durability of Polymer Matrix Composites. 10.1016/B978-0-12-803581-8.10044-X.

52. Yale University. (2021). SEM Principle. [Online]. Available at: https://ywcmatsci.yale.edu/facilities/sem/sem-principle.

53. Chen, Shiyou & Gong, Xiaowu & Walsh, Aron & Wei, Su-Huai. (2010). Defect physics of the kesterite thin-film solar cell absorber Cu2ZnSnS4. Applied Physics Letters. 96. 021902-021902. 10.1063/1.3275796.

54. Ansari, Mohd & Parveen, Nazish & Nandi, Dip & Ramesh, Rahul & Ansari, Sajid & Cheon, Taehoon & Kim, Soo-Hyun. (2019). Enhanced activity of highly conformal and layered tin sulfide (SnSx) prepared by atomic layer deposition (ALD) on 3D metal scaffold towards high performance supercapacitor electrode. Scientific Reports. 9. 10.1038/s41598-019-46679-7.

55. Lakshmi, V. & Chen, Ying & Mikhaylov, Alexey & Medvedev, Alexander & Sultana, Irin & Rahman, Md Mokhlesur & Lev, Ovadia & Prikhodchenko, Petr & Glushenkov, Alexey. (2017). Nanocrystalline SnS 2 coated onto reduced graphene oxide: demonstrating feasibility of a non-graphitic anode with sulfide chemistry for potassium-ion batteries. Chem. Commun.. 53. 10.1039/C7CC03998K.

56. Naïma, T. & Ramdane, M. & Chahrazed, D. (2019). Impact of the secondary phase ZnS on CZTS performance solar cells. Internal Journal of control, Energy and Electrical Engineering (CEEE). Vol 9 pp. 6-9. http://ipco-co.com/CEEE_Journal/CEEE-vol%209/57.pdf.

57. P. K. Nair, J. Cardoso, O. Gomez Daza, and M. T. S. Nair, "Polyethersulfone foils as stable transparent substrates for conductive copper sulfide thin film coatings," Thin Solid Films, vol. 401, no. 1-2, pp. 243–250, 2001.

58. Wang, Lei & Lee, Chong Yong & Schmuki, Patrik. (2013). Solar water splitting: Preserving the beneficial small feature size in porous α-Fe2O3 photoelectrodes during annealing. Journal of Materials Chemistry A. 1. 212-215. 10.1039/C2TA00431C.

59. Coridan, Robert & Nielander, Adam & Francis, Sonja & McDowell, Matthew & Dix, Victoria & Chatman, Shawn & Lewis, Nathan. (2015). Methods for Comparing the Performance of Energy-Conversion Systems for Use in Solar Fuels and Solar Electricity Generation. Energy Environ. Sci.. 8. 10.1039/C5EE00777A.

60. Jiang, Feng & Huang, Dingwang & Wang, Kang & Li, Lintao & Feng, Kuang & An, Na & Ng, Yun Hau & Kuang, Yongbo & Ikeda, Shigeru. (2021). 3.17% efficient Cu2ZnSnS4 -BiVO4 integrated tandem cell for standalone overall solar water splitting. Energy & Environmental Science. 14. 10.1039/D0EE03892J.

List of Figures

List of Tables

List of Symbols

ABPE	Applied bias photon to-current efficiency
APCE	Absorbed photon to current efficiency
CB	Conduction band
CBD	Chemical bath deposition
CCZTS	Cadmium Copper zinc tin sulfide
CIGS	Copper indium gallium diselenide
CZTS	Copper zinc tin sulfide
D	Diffusivity
e	Electrical charge of an electron
Ec	Conduction band energy
EC	Electrochemical catalyst
EDS	Energy dispersive spectroscopy
EF	Fermi energy level
Ei	Fermi energy level in the undoped semiconductor
Egap	Energy band gap
$Eredox$	Redox Potential
EQE	External quantum efficiency
Ev	Valence band energy
FTO	Fluorine-doped tin oxide
FWHM	Full width at half maximum
g	Density of states
h	Plank's constant $(6,626 \times 10\text{-}34)$
HER	Hydrogen reaction evolution

IPCE	Incident photon to current efficiency
IQE	Internal quantum efficiency
J	Current density
K	Shape factor
k_B	Boltzmann's constant (1.38*10-23)
LSV	Linear scan voltammetry
L_D	Diffusion length
m^*	Effective mass
n	Electron concentration
N_A	Concentration of acceptors
N_D	Concentration of donor
N_{eff}	Effective density of states
n_i	Carrier concentration in the undoped semiconductor
OER	Oxygen evolution reaction
p	Holes concentration
PEC	Photoelectrochemical water splitting
PED	Photo electrodeposition
PEM	Proton exchange membrane
PV	Photovoltaic
RHE	Reversible Hydrogen Electrode
SEM	Scan electron microscopy
SHE	Standard hydrogen electrode
STCH	Solar thermochemical hydrogen
STH	Solar to hydrogen efficiency
TF	Fermi Temperature
VB	Valence band
W_{sc}	Depletion width
XRD	X-ray diffraction
$\varphi(x)$	Variation of electrostatic potential

ε_0	Permittivity in vacuum
ε_{SC}	Dielectric constant of semiconductor
θ	Bragg Angle
λ	Wavelength
μ	Mobility
ν	Frequency
σ	Conductivity
τ	Mean free time of recombination
χ	Work function
ϕ	Electric potential below the vacuum level